

DEVELOPMENT OF HPGE DETECTOR  
FOR THE LONGITUDINAL EMITTANCE MEASUREMENT

By

Reiko Taki

A THESIS

Submitted to  
Michigan State University  
in partial fulfillment of the requirements  
for the degree of

MASTER OF SCIENCE

Department of Physics and Astronomy

2003

## ABSTRACT

### DEVELOPMENT OF HPGE DETECTOR FOR THE LONGITUDINAL EMITTANCE MEASUREMENT

By

Reiko Taki

The longitudinal emittance of the beam from the RIKEN Ring Cyclotron (RRC) is indispensable knowledge for the operation of the Radioactive Isotope Beam Factory, which is now under construction and uses the RRC as an injector. We proposed to employ a HPGe detector as a compact and convenient energy detector for longitudinal emittance measurements and studied the feasibility of its use with high-energy heavy ions. A reasonably good energy resolution,  $\delta E/E = 6.5 \times 10^{-4}$ , has been observed for 1890-MeV  $^{14}\text{N}$ , which makes the HPGe promising. A new detector is being fabricated to achieve a better resolution. Also the longitudinal emittances were measured for 3800-MeV  $^{40}\text{Ar}$  and 2420-MeV  $^{22}\text{Ne}$ . It has been demonstrated that the measurement of longitudinal emittance provides rich information on the acceleration condition, such as the single-turn extraction and the effect of phase compression, and is very helpful for the beam tuning of the present and new facilities.

# TABLE OF CONTENTS

<b>1</b>	<b>Introduction</b>	<b>1</b>
1.1	Purpose of Experiment . . . . .	1
1.2	Cyclotron . . . . .	2
1.2.1	Principle of Cyclotron . . . . .	3
1.2.2	Sector Focus Cyclotron . . . . .	5
1.2.3	Beam Extraction . . . . .	7
1.2.4	Single- and Multi-Turn Extraction . . . . .	10
1.2.5	Longitudinal Emittance . . . . .	11
1.2.6	Phase Compression . . . . .	13
1.3	HPGe Detector . . . . .	13
1.3.1	Range of Particles . . . . .	14
1.3.2	Simple Estimation of Energy Resolution . . . . .	15
1.3.3	Energy Loss Straggling . . . . .	16
1.3.4	Recombination Effect . . . . .	19
1.3.5	Radiation Damage . . . . .	19
<b>2</b>	<b>Experimental Arrangement</b>	<b>20</b>

2.1	AVF Cyclotron . . . . .	21
2.2	Ring Cyclotron . . . . .	22
2.3	Beam Transport . . . . .	24
2.4	Target and Collimator . . . . .	27
2.5	Magnetic Spectrometer SMART . . . . .	28
2.6	Detector Systems . . . . .	31
2.6.1	Energy Resolution Measurement . . . . .	31
2.6.2	Longitudinal Emittance Measurements . . . . .	32
2.7	Data Acquisition . . . . .	35
2.7.1	Energy Resolution Measurement . . . . .	35
2.7.2	Longitudinal Emittance Measurements . . . . .	37
<b>3</b>	<b>Analysis</b>	<b>38</b>
3.1	Energy Calibration of HPGe . . . . .	38
3.2	Veto by Active Slit . . . . .	41
3.3	Time Calibration . . . . .	42
3.4	Position Calibration . . . . .	42
3.5	Time of Flight Correction . . . . .	44
<b>4</b>	<b>Results and Discussions</b>	<b>50</b>
4.1	Energy Resolution of HPGe . . . . .	50
4.2	Longitudinal Emittance of $^{40}\text{Ar}$ Beam — case of single turn extraction — . . . . .	52
4.3	Longitudinal Emittance of $^{22}\text{Ne}$ Beam — case of multi-turn extraction — . . . . .	58

<b>5</b>	<b>Conclusions</b>	<b>62</b>
<b>6</b>	<b>Future Prospects</b>	<b>64</b>
	<b>Appendix</b>	<b>66</b>
<b>A</b>	<b>Angular Distribution of Elastic Scattering</b>	<b>67</b>

# LIST OF TABLES

1.1	Ranges of Ge for typical beams delivered from the RRC. . . . .	15
1.2	Estimation of energy loss straggling for some materials. . . . .	18
2.1	List of the experiments. . . . .	20
2.2	Accelerator parameters. . . . .	24
2.3	Energy spreads due to the angular acceptance of the collimator $\Delta E_{\text{ang}}$ and the energy-loss straggling in the target $\Delta E_{\text{straggle}}$ (FWHM). . . . .	28
2.4	Typical optical characteristics of the SMART. . . . .	29
3.1	Energies of $\gamma$ rays emitted by $^{60}\text{Co}$ , $^{22}\text{Na}$ , $^{137}\text{Cs}$ and $^{40}\text{Kr}$ , and the corresponding ADC channels. . . . .	40
4.1	Peak width in observed energy spectra, the contributions from energy- loss straggling and the intrinsic energy resolution of HPGe at normal and $43^\circ$ injections for 1890-MeV $^{14}\text{N}$ . . . . .	51
6.1	Specifications of Ge detector (Princeton Gammatech: IGP1010185 Model). . . . .	65

# LIST OF FIGURES

1.1	Schematic layout of the new facility, RIBF, at RIKEN. . . . .	1
1.2	Schematic drawings of the cyclotron. Vertical (left) and horizontal (right) mid plane cross sections. . . . .	3
1.3	Schematic drawings of AVF (upper panel) and Ring (lower panel) cyclotrons at RIKEN. Both of them have four sectors. . . . .	6
1.4	Beam current versus radius measured with the differential probe for a 135-MeV/ $A$ $^{28}\text{Si}^{14+}$ beam at the RRC. . . . .	9
1.5	Kinetic energy versus RF phase near extraction (solid curve) and energy profile of the extracted beam for the case of multi-turn extraction (dots). . . . .	10
1.6	$(T, t)$ correlation of 185-MeV Ar beam measured at VICKSI (presently ISL), Hahn-Meitner Institute [4]. The right panel shows a high-resolution measurement (presumably, labels on abscissa, 84.8 and 85.0, should read 184.8 and 185.0). . . . .	11
1.7	$(T, \phi)$ correlation of the extracted beam for the case of single-turn extraction. Injection phases are displaced by $0^\circ$ , $\pm 3^\circ$ and $\pm 6^\circ$ around $\phi_0$ . . . . .	12
2.1	Schematic layout of RIKEN Accelerator Research Facility. . . . .	21
2.2	Dependence of acceleration voltage on the relative phase $\phi$ . . . . .	22
2.3	Beam configuration in the RRC in the case of the AVF injection. . . . .	24
2.4	Transport line components from the RRC to F2 of SMART together with the extraction components of the RRC. . . . .	25

2.5	A Typical beam envelope from the RRC to the target of scattering chamber in E4 experimental area. . . . .	26
2.6	Side view of the SMART scattering chamber. . . . .	27
2.7	Arrangement of SMART and the detector system. . . . .	30
2.8	Setup of the HPGe detector and the slits for the energy resolution measurement. . . . .	31
2.9	Setup of Si-PSD and the plastic scintillators for the longitudinal emittance measurements. . . . .	33
2.10	A simplified equivalent circuit and the layout of Si-PSD. . . . .	34
2.11	Data acquisition system for the energy resolution measurement. . . .	36
2.12	Data acquisition system for the longitudinal emittance measurements.	36
3.1	Energy spectra from $^{137}\text{Cs}$ , $^{22}\text{Na}$ and $^{60}\text{Co}$ sources which are used for the energy calibration of ADC channels. The peak from the background, $^{40}\text{K}$ , was also observed. . . . .	39
3.2	Energy spectra for all events (unshaded) and for events without signals from the active slit (shaded). . . . .	41
3.3	Typical time spectrum used for time calibration (upper panel). Pulses from a time calibrator had a 10 ns interval over 100 ns range. The regression line is shown in the lower panel. . . . .	42
3.4	Spectrum used for calibration of Left ADC (upper panel). The regression line is shown in the lower panel. . . . .	43
3.5	$Q_{\text{left}}-Q_{\text{right}}$ plot for different $x$ generated by the dedicated position calibrator. The inset is a closeup around the intersecting point. . . . .	44
3.6	Spectrum of $x/L$ calculated by using Eq. (2.5) (upper panel). Discrete peaks reflecting the strip structure are clearly seen. The lower panel shows the regression curve to deduce the correct position determined by the least squares method. . . . .	45
3.7	Time spectra with the first-term correction only. The injection phase with respect to the RF phase of the RRC, $\Delta\phi_{\text{inj}}$ , is displaced in step of $2^\circ$ . . . . .	47

3.8	Same as Fig. 3.7but with the correction assuming $(l \delta) = -35.5$ cm/%.	47
3.9	The correlation between the time and momentum of particles detected at F2 without the stripper (left) and with the stripper (right).	48
3.10	Beam spot on a ZnS scintillation target at the target position with (right panel) and without the stripper foil (left panel). Ticks on the target are marked in 5 mm step.	49
4.1	Energy spectra with the active slit at normal and $43^\circ$ injections, respectively.	50
4.2	Longitudinal emittances of 3800-MeV $^{40}\text{Ar}$ . The injection phase $\Delta\phi_{\text{inj}}$ is displaced relative to the RF of the RRC in step of $2^\circ$ .	53
4.3	Schematic illustration of phase compression effect for the case of narrow-bunched beam. The extraction time is either relative to the RF of the RRC (upper panel) or relative to the injection (lower panel).	55
4.4	Projected spectra of the extraction time relative to the injection. The phase of the RF with respect to the injection, $\Delta\phi_{\text{inj}}$ , is shifted in step of $2^\circ$ .	56
4.5	Shifts of time spectra deduced from Fig. 4.4 plotted as a function of $\Delta\phi_{\text{inj}}$ . The solid line is a prediction from Eq. (1.13). The dashed curve is a third order polynomial for eye-guide.	57
4.6	Time spectrum (upper panel), the longitudinal emittances for the main and adjacent turns at the nominal Dee voltage (middle panels) and at a slightly lowered Dee voltage (lower panels). Straight lines are for eye-guide.	59
4.7	Schematic illustration of $\delta T$ - $\delta t$ correlations for neighboring turns at the nominal Dee voltage (upper panel) and at a slightly lowered Dee voltage (lower panel).	60
6.1	Overview of the newly fabricated HPGe detector.	65
A.1	Angular distribution of $^{197}\text{Au}(^{14}\text{N}, ^{14}\text{N})^{197}\text{Au}$ elastic scattering at $E/A = 135$ MeV/A compared with Rutherford scattering. The exponential line is for eye-guide.	68

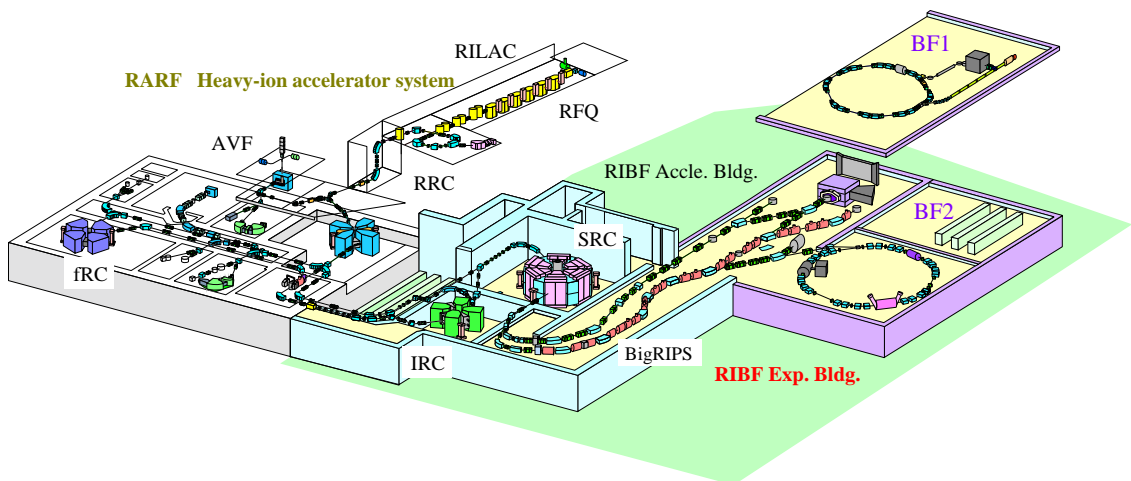
# Chapter 1

## Introduction

### 1.1 Purpose of Experiment

The new facility, Radioactive Isotope Beam Factory (RIBF), is now under construction at RIKEN and is scheduled to be operational in 2006. The schematic layout of the facility is shown in Fig. 1.1. The main accelerator of the present facility, RIKEN Ring Cyclotron (RRC), will be used as a pre-accelerator in this new facility. The typical injection energy is 60 MeV/A, although the RRC is capable to accelerate up

**RI Beam Factory (RIBF): Upgrading project of RIKEN Accelerator Research Facility (RARF)**



RIBF RI beam experiments will be started in 2006.

Figure 1.1: Schematic layout of the new facility, RIBF, at RIKEN.

to 135 MeV/A for  $Z/A = 1/2$  particles.

For designing new accelerator components, such as a re-buncher after the RRC, the information of time structure and energy spread, i.e., the longitudinal emittance of the beam coming from the RRC is needed. For successful operation of this accelerator complex, it is also important to know the longitudinal emittance while beam tuning. Because the typical time and relative energy spreads of the beam coming from the RRC are 1 ns and  $10^{-3}$ , the required time and energy resolutions for the measurement are  $\delta t \simeq 0.1$  ns and  $\delta E/E \simeq 10^{-4}$ , respectively. Such an energy resolution is usually achieved by using a magnetic spectrometer, but, for the routine beam tuning, the use of a compact and convenient detector system is more desirable. We propose to employ a High Purity Germanium (HPGe) detector for this purpose. The response of HPGe to medium energy protons,  $\leq 150$  MeV, was reported, for example in Ref. [10], but that to energetic heavy ions is not well known. In the present experiment, the energy resolution of HPGe has been studied for 135-MeV/A  $^{14}\text{N}$ , the momentum of which is defined by using a magnetic spectrometer. We also studied the longitudinal emittances of 95-MeV/A  $^{40}\text{Ar}$  and 110-MeV/A  $^{22}\text{Ne}$  beams.

## 1.2 Cyclotron

Cyclotron is a circular particle accelerator first built by Lawrence and Livingston in 1930. The cyclotron employs a uniform magnetic field to guide particles along the circular orbit, so that particles can be accelerated many times by the same accelerating cavities. The principle of the cyclotron, however, is limited to non-relativistic particles because of the change of revolution frequency. The technique of varying the radio frequency (RF) of the accelerating cavity overcomes this limitation. This is the principle of synchrocyclotron. In 1938, a significant breakthrough, strong focusing, came out from H. A. Thomas. He found that the radial dependence of the magnetic

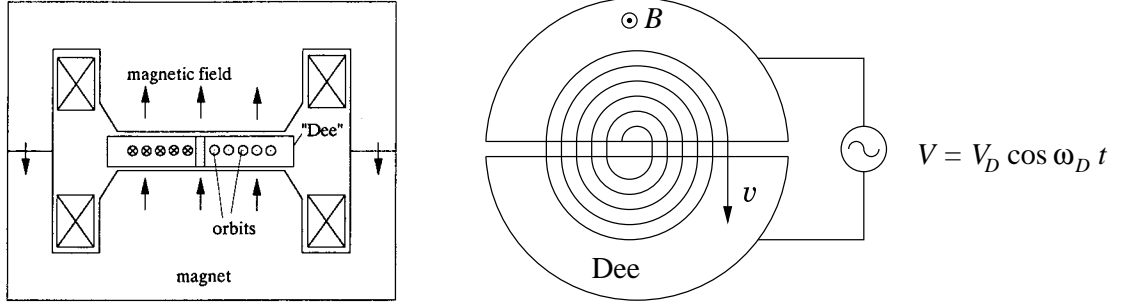


Figure 1.2: Schematic drawings of the cyclotron. Vertical (left) and horizontal (right) mid plane cross sections.

field makes the revolution frequency of particles constant. The machine employing this principle is called isochronous cyclotron. In contrast to the synchrocyclotron, the isochronous cyclotron provides a continuous thus high-intensity beam. Presently, most of cyclotrons are isochronous type. Details of cyclotrons as well as other types of accelerators can be found in textbooks, e.g., Refs. [1] and [2].

### 1.2.1 Principle of Cyclotron

The schematic configuration of an early cyclotron is shown in Fig. 1.2. The cyclotron consists of magnets which generate a uniform magnetic field and two accelerating cavities which extend over the whole aperture between the poles. These cavities form semi-circles and generate the accelerating fields between them. Because of its shape, the cavity is often called *Dee*. Since particles travel inside Dees, they are contained in a vacuum box. The magnets have coils surrounding their poles and yokes which reduce leakage field and resistance of magnetic field.

A particle which has the charge  $q$  and is moving at the velocity of  $\mathbf{v}$  in the electric and magnetic fields,  $\mathbf{E}$  and  $\mathbf{B}$ , feels the Lorentz force,

$$\mathbf{F} = q (\mathbf{E} + \mathbf{v} \times \mathbf{B}) . \quad (1.1)$$

Particles injected from the center of the cyclotron perpendicularly to the uniform

magnetic field  $\mathbf{B}$  are guided along a circular orbit. Under this condition, Eq. (1.1) is reduced to

$$F = qvB .$$

An equilibrium between Lorentz force and the centrifugal force,

$$\frac{m\gamma v^2}{r} = qvB ,$$

defines the curvature of the orbit  $r$  as

$$r = \frac{p}{qB} , \tag{1.2}$$

where  $m$  and  $p$  are the mass and momentum of the particle, respectively.  $\gamma$  is the Lorentz factor defined by  $\gamma = 1/\sqrt{1-(v/c)^2}$ . Particles are accelerated by an electric field  $E$  every time when passing the gap between the accelerating cavities. Because the momentum of the particle  $p$  increases after acceleration, the curvature of the orbit  $r$  becomes larger and larger. Accordingly, the orbit of the particle forms in spiral. The revolution time  $\tau$  and the revolution frequency  $f_{\text{rev}}$  are given by

$$\tau = \frac{2\pi r}{v} = \frac{2\pi p}{qB v} = \frac{2\pi m\gamma}{qB} = \frac{1}{f_{\text{rev}}} . \tag{1.3}$$

They remain constant for non-relativistic case, where  $\gamma \simeq 1$ . The accelerating voltage  $V(t)$  applied to the cavities is a sinusoidal function,

$$V(t) = V_D \cos \omega_D t . \tag{1.4}$$

The angular velocity  $\omega_D = 2\pi f_{\text{rf}}$  is chosen in such a way that the particles get the

maximum energy gain  $qV_D$  when passing the accelerating gaps. This condition entails

$$f_{\text{rf}} = hf_{\text{rev}} = h \frac{qB}{2\pi m\gamma}, \quad (1.5)$$

where  $h$  is an integer called harmonic number. When the particles' velocities become relativistic,  $\gamma > 1$ , the revolution frequency  $f_{\text{rev}}$  becomes smaller and smaller during acceleration and the particles get out of synchronism with  $f_{\text{rf}}$ . This is a reason why the early cyclotron is limited to non-relativistic particles. Maximum kinetic energy  $T_{\text{max}}$  obtained by acceleration is often represented by using  $K$ -value as

$$T_{\text{max}} = K \frac{Q^2}{A},$$

where  $A$  and  $Q$  are the atomic mass of the particle and its charge in units of  $e$ , respectively. For non-relativistic case,  $K$  can be expressed as

$$K = \frac{(rB)^2}{2} \frac{e^2}{m_u},$$

where  $m_u$  is the atomic mass unit.

### 1.2.2 Sector Focus Cyclotron

The sector focus cyclotron can accelerate relativistic particles using a constant  $f_{\text{rf}}$  by adjusting the magnetic field  $B$ . According to Eq. (1.5), the required modulation of magnetic field is given by

$$B(r) = B_0\gamma, \quad (1.6)$$

where  $B_0$  is a magnetic field in the central region of the cyclotron. This equation indicates that the magnetic field  $B$  must increase with  $r$  in proportion to  $\gamma$ . Such a

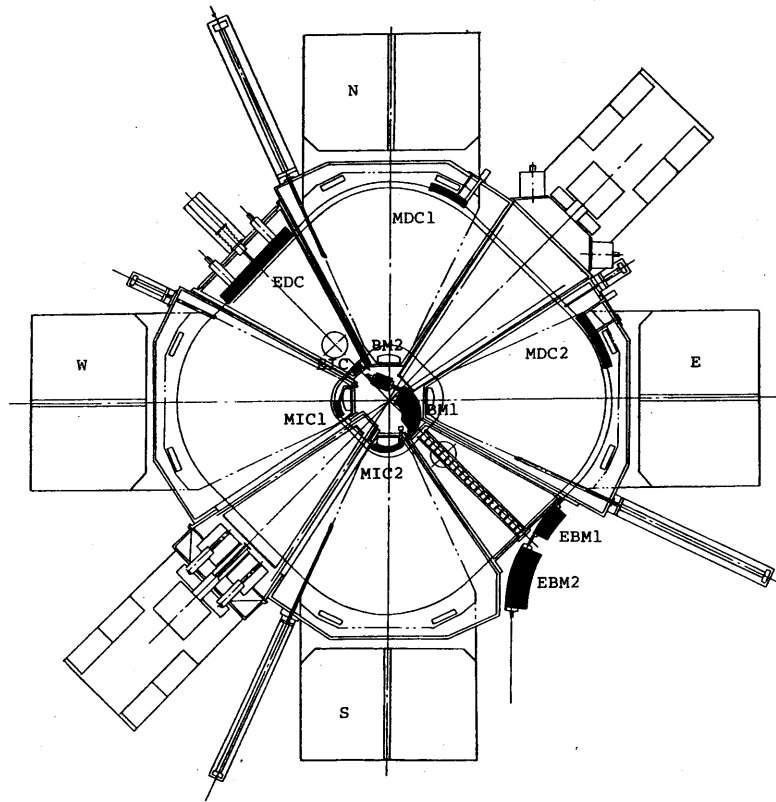
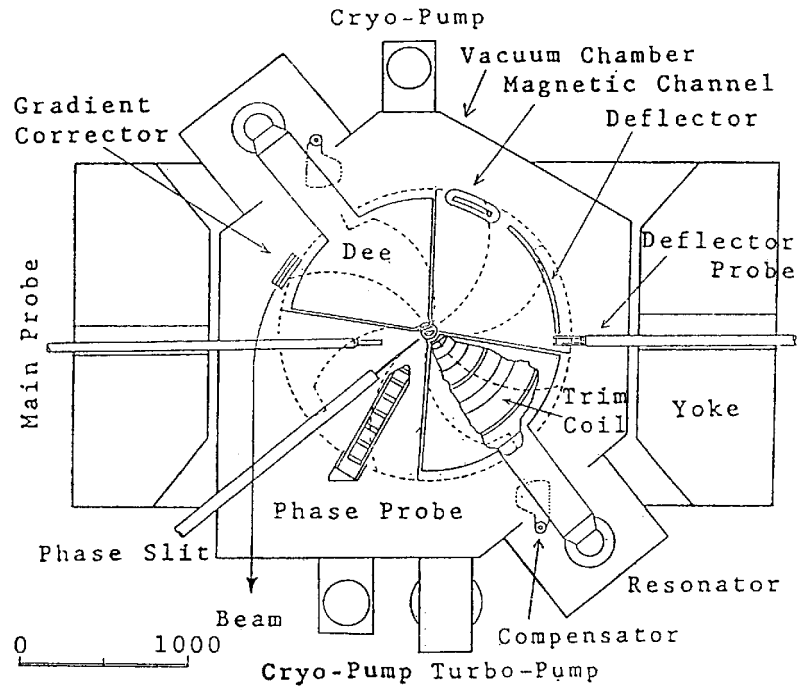


Figure 1.3: Schematic drawings of AVF (upper panel) and Ring (lower panel) cyclotrons at RIKEN. Both of them have four sectors.

field, however, causes a vertical defocusing of particles, while it provides a horizontal focusing. This vertical instability can be compensated by an azimuthally alternating varying field. Focusing powers arise at the boundaries between strong and weak fields. These fields can be formed by hill and valley on the poles. This type of machine is called azimuthally varying field (AVF) cyclotron (upper panel of Fig. 1.3). The larger difference of field strength makes the stronger focusing power. In order to provide a maximumly varying field, the magnets are divided into some sectors as shown in lower panel of Fig 1.3. Accelerating cavities are arranged in the field-free regions, where much more spaces are available than magnet regions. Thus the cavities can be designed to have higher quality factors and generate the RFs with higher voltages. The orbit of particles becomes quadrangle-like because the particles go straight in the field-free regions while they curve in the magnetic fields. The average of magnetic fields in each turn,

$$\langle B(r) \rangle = \frac{1}{2\pi} \int_0^{2\pi} B(r, \theta) d\theta ,$$

must satisfy Eq. (1.6) to keep the isochronal condition, where  $\theta$  is the azimuth.

### 1.2.3 Beam Extraction

Several kinds of extraction methods are employed for cyclotrons [3]. Generally in the case of positive ion acceleration, the beams can be extracted with the help of extraction devices such as electrostatic and magnetic deflector channels (EDC and MDC). The EDC consists of a septum, which is a thin inner electrode at the earth potential, and an outer electrode at a negative high potential. Reaching the final radius, particles enter between the septum and the outer electrode to be directed away from the cyclotron magnetic field. In order to reduce the cyclotron magnetic field along the extraction path, MDCs are employed. In the design of MDC, it is

important to keep the stray magnetic field as small as possible in the area of the last acceleration orbit. For achieving a high extraction efficiency and a good beam quality, a large separation between successive turns is desired. The radial position of a particle at an azimuth  $\theta$  in the cyclotron is given by

$$r(\theta) = r_0(\theta) + x(\theta) \sin(\nu_r \theta + \theta_0), \quad (1.7)$$

where  $r_0(\theta)$  is the radial position of the equilibrium orbit at that azimuth,  $x(\theta)$  is the radial oscillation amplitude and  $\theta_0$  is an arbitrary phase angle.  $\nu_r$  is a betatron tune defined as the number of cycles of the radial oscillation during one turn. For incoherent oscillations, the amplitude  $x(\theta)$  is given by

$$\sqrt{\beta_{r_0}(\theta) \epsilon_x},$$

where  $\beta_{r_0}$  is the radial beta function for radius  $r_0$  and at azimuth  $\theta$ , and  $\epsilon_x$  the radial emittance. Rewriting Eq. (1.7) as a function of turn number  $n$ , the radial position at a fixed azimuth  $\theta_i = 2\pi n$  becomes

$$r(\theta_i) = r_0(\theta_i) + x(\theta_i) \sin(2\pi n(\nu_r - 1) + \theta_0), \quad (1.8)$$

where for convenience  $\nu_r - 1$  has been taken since  $\nu_r$  is close to 1, which is the case with most isochronous cyclotrons. The separation between two successive turns is given by

$$\begin{aligned} \Delta r(\theta_i) &= \Delta r_0(\theta_i) + \Delta x \sin(2\pi n(\nu_r - 1) + \theta_0) \\ &\quad + 2\pi(\nu_r - 1)x \cos(2\pi n(\nu_r - 1) + \theta_0). \end{aligned} \quad (1.9)$$

The first term on the right-hand side in Eq. (1.9) represents the orbit separation due to acceleration. Using the kinetic energy of particle  $T = \sqrt{(mc^2)^2 + (pc)^2} - mc^2$  and Eq. (1.2), the turn separation due to acceleration becomes

$$\frac{\Delta\bar{r}}{\bar{r}} = \frac{\gamma}{\gamma+1} \frac{\Delta T}{T}, \quad (1.10)$$

where  $\bar{r}$  and  $\Delta T$  are the average radius and the energy gain per turn, respectively. The second term in Eq. (1.9) gives the orbit separation by an increase in the oscillation amplitude. This can be accomplished by providing a gradient of first harmonic magnetic field, which leads to an increase in the beta function  $\beta_{r0}$ . This method is called regenerative extraction. The third term in Eq. (1.9) describes a turn separation due to precessional orbit motion with the oscillation amplitude  $x$ . The maximum turn separation produced by the precessional motion is given by  $2\pi(\nu_r - 1)x$ . The extraction using the precessional orbit motion is called precessional extraction. It can be achieved by off-center injection, which generates a rotation of the orbit center around the machine center, and thus, the oscillation pattern of the radius. A typical turn separation is presented in Fig. 1.4.

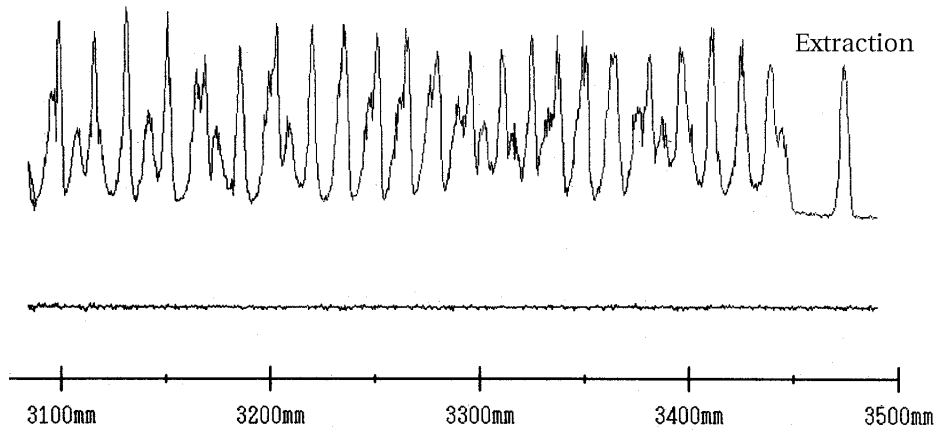


Figure 1.4: Beam current versus radius measured with the differential probe for a 135-MeV/A  $^{28}\text{Si}^{14+}$  beam at the RRC.

### 1.2.4 Single- and Multi-Turn Extraction

In general, particles with a different value of the accelerating RF phase experience a different number of turns before reaching the extraction radius. In a purely isochronous cyclotron, RF phase of a particle remains constant. This leads to the multi-turn extraction. The single-turn extraction can be achieved by restricting the injection RF phase with a help of phase slits in the central region of cyclotron. This reduces the energy spread of the extracted beam. The flat-top technique is also useful, as described later. The kinetic energy  $T$  and the radius  $r$  of a particle on an ideal orbit with accelerating voltage  $V(t)$  in Eq. (1.4) are

$$T(\phi) = T_0 \cos \phi \simeq T_0 \left(1 - \frac{1}{2} \phi^2\right) \quad (1.11)$$

$$r(\phi) = r_0 \sqrt{\frac{T(T+2mc^2)}{T_0(T_0+2mc^2)}} \simeq r_0 \left[1 - \frac{1}{2} \frac{\gamma}{\gamma+1} \phi^2\right],$$

where  $T_0$  and  $r_0$  are the kinetic energy and radius at the central RF phase  $\phi_0$ , and  $\phi$  is the phase difference with respect to  $\phi_0$ . Figure 1.5 shows the energies for orbits near

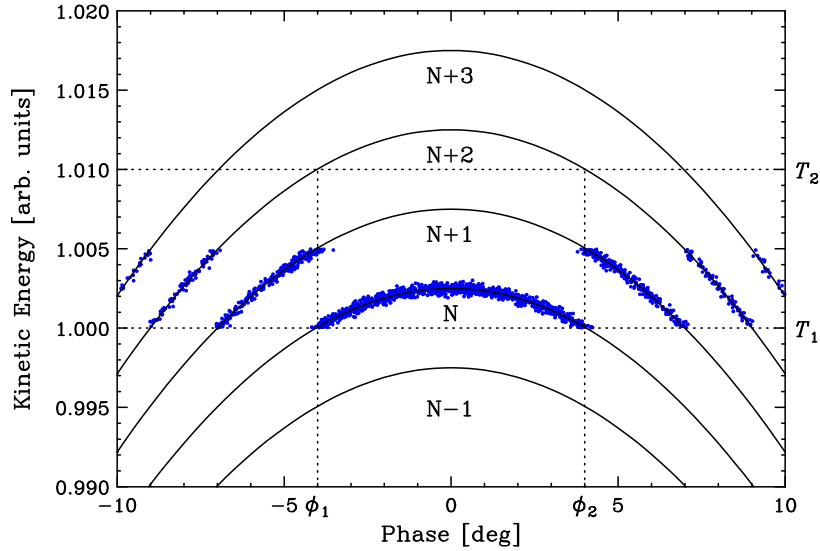


Figure 1.5: Kinetic energy versus RF phase near extraction (solid curve) and energy profile of the extracted beam for the case of multi-turn extraction (dots).

extraction and the energy pattern of the extracted beam as a function of RF phase. It is seen that several turns get extracted when an energy gate opens between  $T_1$  and  $T_2$ , which are mainly defined by the EDC and MDC apertures. The single-turn extraction can be accomplished by restricting phase width  $\leq \phi_2 - \phi_1$ . This is further discussed for an actual case in Sec. 4.3.

### 1.2.5 Longitudinal Emittance

The motion of each particle at any given time is defined by the space coordinate  $(x, y, z)$  and the momentum coordinate  $(p_x, p_y, p_z)$ . Here the beam is assumed to propagate in the  $z$ -direction. Particles in a beam occupy a certain region in phase space which is called the beam emittance. The concept of describing a particle beam in phase space is very powerful because the density of particles in phase space does not change along a beam transport line (Liouville's theorem). Since the coupling between

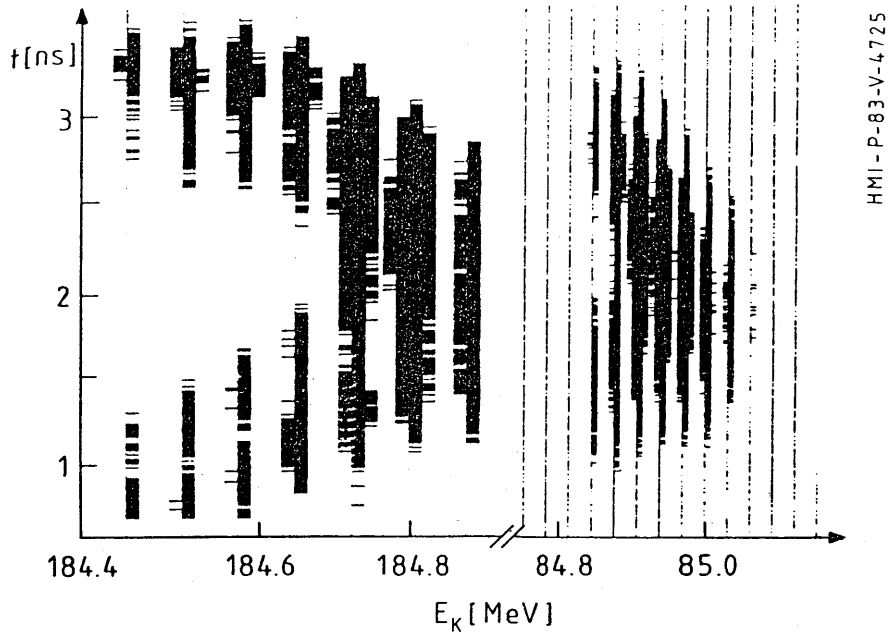


Figure 1.6:  $(T, t)$  correlation of 185-MeV Ar beam measured at VICKSI (presently ISL), Hahn-Meitner Institute [4]. The right panel shows a high-resolution measurement (presumably, labels on abscissa, 84.8 and 85.0, should read 184.8 and 185.0).

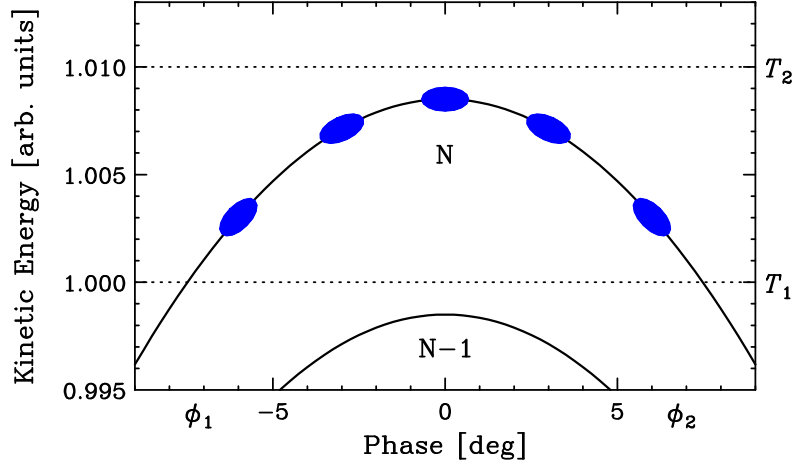


Figure 1.7:  $(T, \phi)$  correlation of the extracted beam for the case of single-turn extraction. Injection phases are displaced by  $0^\circ$ ,  $\pm 3^\circ$  and  $\pm 6^\circ$  around  $\phi_0$ .

the transverse and longitudinal motion, as well as the coupling between the horizontal and vertical plane, is being ignored in linear beam dynamics, six-dimensional phase space can be split into three independent two-dimensional phase planes. In systems where the beam energy stays constant, the slopes of the trajectory  $a \equiv p_x/p$  and  $b \equiv p_y/p$  may be used instead of the transverse momenta and the transverse emittances are usually defined as areas in  $x$ - $a$  and  $y$ - $b$  planes. Likewise the longitudinal emittance is defined as an area in  $z$ - $p$  plane or, as another set of canonically conjugate variables, in  $t$ - $T$  plane. The area alone, however, does not reflect the detailed quality of the beam thus we will rather discuss the *longitudinal distribution* in  $t$ - $T$  plane.

The beam extracted from the cyclotron is expected to have a quadratic correlation between  $T$  and  $\phi$ , or equivalently time  $t$ , according to Eq. (1.11). Such a correlation was actually measured at several facilities [4, 5]. An example at VICKSI (presently ISL), Hahn-Meitner Institute, is shown in Fig. 1.6.

The phase width of the injection beam is often reduced by using a phase slit and a buncher so that the single-turn is extracted easily. In this case, the quadratic correlation is not observed, but it is useful to intentionally displace the injection phase to see the correlation and to diagnose the acceleration condition conveniently (Fig. 1.7). This method is employed in the present experiment for  $^{40}\text{Ar}$  case (Sec. 4.2).

### 1.2.6 Phase Compression

The phase compression was first mentioned by Müller and Mahrt [6] and generalized in Ref. [7]. A radial voltage distribution of the RF cavity produces a time varying magnetic field. This field compresses the bunch size of beam for a radially increasing voltage or expands it for a radially decreasing voltage. For an ideal isochronous cyclotron, the effect of phase compression can be described by the Hamiltonian

$$H(T(n), \phi(n)) = qV(n) \sin \phi(n) ,$$

where  $\phi(n)$  is the relative phase and  $qV(n)$  is the peak energy gain per turn at  $n$ -th turn. Since the Hamiltonian  $H$  does not depend explicitly on the turn number  $n$  ( $\partial H/\partial n = 0$ ), it is a constant of motion. This leads to an important relation between peak energy gain and relative phase of acceleration,

$$qV(n_1) \sin \phi(n_1) = qV(n_2) \sin \phi(n_2) , \quad (1.12)$$

where  $n_1$  and  $n_2$  are turn numbers in an isochronous cyclotron. According to this equation, a voltage distribution increasing from  $V_{\text{inj}}$  at injection to  $V_{\text{ext}}$  at extraction can compress the original phase spread  $\phi_{\text{inj}}$  into

$$\phi_{\text{ext}} = \frac{V_{\text{inj}}}{V_{\text{ext}}} \phi_{\text{inj}} . \quad (1.13)$$

## 1.3 HPGe Detector

In this section, matters related to operation of HPGe detectors are described. Detailed review of them can be found in textbooks, e.g., Refs. [8] and [9].

### 1.3.1 Range of Particles

Heavy charged particles lose their energy by Coulomb interaction with the electrons and the nuclei of absorbing materials. The collisions of heavy charged particles with the free and bound electrons of the material are mainly responsible for the energy loss of heavy particles and result in the ionization or excitation of the atom. The scattering from nuclei also occurs, although not as often as electron collisions. Thus the major part of the energy loss is due to electron collisions. The average energy loss per unit path length,  $\frac{dE}{dx}$ , was calculated by Bethe and Bloch. The Bethe-Bloch formula is

$$-\frac{dE}{dx} = 2\pi N_a r_e^2 m_e c^2 \rho \frac{Z}{A} \frac{z^2}{\beta^2} \left[ \ln \left( \frac{2m_e \gamma^2 v^2 W_{\max}}{I^2} \right) - 2\beta^2 \right], \quad (1.14)$$

where

$$2\pi N_a r_e^2 m_e c^2 = 0.1535 \text{ MeV cm}^2/\text{g}$$

$$N_a : \text{Avogadro's number} = 6.022 \times 10^{23} \text{ mol}^{-1}$$

$$r_e : \text{classical electron radius} = 2.817 \times 10^{-23} \text{ cm}$$

$$m_e : \text{electron mass} = 0.511 \text{ MeV}/c^2$$

$$Z : \text{atomic number of absorbing material}$$

$$A : \text{atomic weight of absorbing material}$$

$$\rho : \text{density of absorbing material}$$

$$z : \text{charge of incident particle in units of } e$$

$$W_{\max} \simeq 2m_e c^2 \eta^2 : \text{maximum energy transfer in a single collision}$$

$$\beta = \frac{v}{c} \text{ of the incident particle}$$

$$\eta = \beta \gamma .$$

The mean range of a particle with a given energy  $E_0$  is obtained by integrating the inverse of Bethe-Bloch formula over  $E$ ,

$$R(E_0) = \int_0^{E_0} \left( \frac{dE}{dx} \right)^{-1} dE. \quad (1.15)$$

The ranges in Ge for some typical beams calculated by Eq. (1.15) are listed in Table 1.1. The result indicates that the HPGe detector with thickness of 1 cm, which is easily obtained commercially, can stop the beams of 60 MeV/ $A$  and serve as an energy detector for the present purpose.

Table 1.1: Ranges of Ge for typical beams delivered from the RRC.

$E/A = 135 \text{ MeV}/A$			$E/A = 60 \text{ MeV}/A$		
Particle	Energy [MeV]	Range [cm]	Particle	Energy [MeV]	Range [cm]
$\alpha$	540	3.798	$\alpha$	240	0.920
$^{12}\text{C}^{6+}$	1620	1.265	$^{12}\text{C}^{6+}$	720	0.307
$^{14}\text{N}^{7+}$	1890	1.084	$^{14}\text{N}^{7+}$	840	0.263
$^{16}\text{O}^{8+}$	2160	0.949	$^{16}\text{O}^{8+}$	960	0.231
$^{20}\text{Ne}^{10+}$	2700	0.760	$^{20}\text{Ne}^{10+}$	1200	0.186
$^{28}\text{Si}^{14+}$	3780	0.546	$^{28}\text{Si}^{14+}$	1680	0.136
$^{40}\text{Ar}^{18+}$	5400	0.477	$^{40}\text{Ar}^{18+}$	2400	0.122

### 1.3.2 Simple Estimation of Energy Resolution

The intrinsic energy resolution  $\delta\epsilon$  depends on the number of electron-hole pairs produced by incoming beam and the Fano factor. Assuming that all the energy deposited by radiation  $E$  is used to create electron-hole pairs and that the number of those pairs  $n$  follows the Poisson distribution, the expected relative energy resolution  $\delta\epsilon/E$  can be obtained by

$$\frac{\delta\epsilon}{E} = 2.35\sqrt{\frac{F}{n}} = 2.35\sqrt{\frac{Fw}{E}}, \quad (1.16)$$

where  $n = E/w$  and  $w$  is the average energy for electron-hole creation, which is 2.96 eV for Ge at 77 K. The Fano factor  $F$  is still not well determined, but is about 0.12. The total energy resolution  $\delta E$  contains contributions from other sources, e.g., electronics noise and fluctuation of leakage current. Denoting them by  $D$ , the resolution can be expressed as

$$\delta E = \sqrt{\delta\epsilon^2 + D^2}. \quad (1.17)$$

A simple estimation of energy resolution is obtained by neglecting  $D$  and by using certification values given in catalogs of commercial products. For example, the DGP100-15 planer-type Ge detector of EURISIS MEASURES Inc., a typical charged-particle detector with thickness of 15 mm and sensitive area of 100 mm<sup>2</sup>, has an energy resolution of  $\delta E_0 = 20$  keV (FWHM) for  $\alpha$  particles with  $E_0 = 5.486$  MeV. On the assumption that  $\delta\epsilon_0 = \delta E_0$ , the relative energy resolution for 1890-MeV <sup>14</sup>N becomes

$$\frac{\delta\epsilon}{E} = \sqrt{\frac{E_0}{E} \frac{\delta\epsilon_0}{E_0}} = 1.96 \times 10^{-4} \text{ (FWHM)}.$$

This value makes HPGe very promising for the present purpose.

### 1.3.3 Energy Loss Straggling

In the measurement of heavy ions, one of major source of  $D$  is the energy loss straggling in the entrance window of the detector, typically made of Be, and in other materials which particles pass through. The amount of energy loss is not equal to the mean energy loss because of the statistical fluctuations in the number of collisions of charged particles with electrons and in the energy transferred in each collision. Therefore, after passing through a fixed thickness of material, an initially mono-energetic beam has an energy distribution. Calculating the distribution of energy losses for a given thickness of absorber is generally divided into two cases: thick absorbers and

thin absorbers.

For relatively thick absorbers, where the number of collisions is large, the total energy loss distribution will approach the Gaussian form,

$$f(x, \Delta) \propto \exp\left[-\frac{(\Delta - \bar{\Delta})^2}{2\sigma^2}\right],$$

where  $x$  is the thickness of the absorber,  $\Delta$  is the energy loss in the absorber,  $\bar{\Delta}$  is the mean energy loss, and  $\sigma$  is the standard deviation. In the case of relativistic heavy ions, the spread  $\sigma$  of this Gaussian can be calculated by

$$\sigma^2 = \frac{(1 - \frac{1}{2}\beta^2)}{1 - \beta^2} \sigma_0^2 \quad \text{and} \quad (1.18)$$

$$\sigma_0^2 = 4\pi N_a r_e^2 (m_e c^2)^2 \rho \frac{Z}{A} x = 0.1569 \rho \frac{Z}{A} x \text{ [MeV}^2\text{]}, \quad (1.19)$$

where  $\sigma_0$  is the spread of the Gaussian for non-relativistic heavy ions,  $N_a$  is Avogadro's number,  $r_e$  and  $m_e$  are the classical electron radius and mass, and  $\rho$ ,  $Z$  and  $A$  are the density, atomic number and atomic weight of the absorber, respectively.

For thin absorbers or gases, where the number of collisions is small, the distribution of energy loss is complicated to calculate because of the possibility of large energy transfers in a single collision. Since a long tail is added to the high energy side of the energy loss probability distribution, the mean energy loss no longer corresponds to the peak. One basic calculation of this distribution was carried out by Vavilov. According to Vavilov's theory, the spread  $\sigma$  is given by

$$\sigma^2 = \frac{\xi^2}{\kappa} \frac{1 - \beta^2}{2}, \quad (1.20)$$

where  $\kappa = \bar{\Delta}/W_{\max}$  and  $\bar{\Delta} \simeq \xi = 2\pi N_a r_e^2 m_e c^2 \rho \frac{Z}{A} \frac{z^2}{\beta^2} x$ , which is the approximated mean energy loss obtained by taking only the first term and ignoring the logarithmic term in Eq. (1.14). Vavilov's formula agrees with Eq. (1.18) for heavy particles.

Substituting  $\kappa$  and  $\xi$  to Eq. (1.20),  $\sigma$  is reduced to

$$\sigma = Cz, \quad \text{where}$$

$$C = \left[ 2\pi N_a r_e^2 m_e^2 c^4 \rho \frac{Z}{A} x \right]^{\frac{1}{2}}.$$

The energy loss straggling caused in a thin absorber is in proportion to the charge of incident particle, but independent of the injecting energy  $E$ . Thus the relative energy spread  $\sigma/E$  becomes larger with  $E$  decreasing. It may be useful to rewrite the formula as

$$\frac{\sigma}{E} = C \frac{z}{A_{\text{in}}} \bigg/ \frac{E}{A_{\text{in}}}.$$

Thus, for incident particles having the same injection energy per nucleon and the same charge-to-mass ratio  $z/A_{\text{in}}$ , the relative energy spread becomes constant.

Table 1.2: Estimation of energy loss straggling for some materials.

Energy [MeV/ $A$ ]	thickness [ $\mu\text{m}$ ]	$\delta E/E$ = $2.35\sigma/E$
Be window		
135	300	$0.38 \times 10^{-3}$
135	25	$0.11 \times 10^{-3}$
60	25	$0.25 \times 10^{-3}$
Plastic Scintillator		
135	100	$0.18 \times 10^{-3}$
60	100	$0.41 \times 10^{-3}$

Table 1.2 shows the energy loss straggling estimated for some materials. The plastic scintillator is used as a timing detector. Since its contribution is relatively large even with a thickness as thin as 100  $\mu\text{m}$ , the use of a micro-channel plate combined with a thin foil for secondary electron production may be considered. Contributions from the vacuum window (Mylar, aramid, etc.), as well as the gold target which is used for elastic scattering, must be also taken into consideration.

### 1.3.4 Recombination Effect

Another possible source of  $D$  in Eq. (1.17) is the recombination effect. In the measurement of heavy ions, the high density of charge carriers created along the ion tracks can decrease the local electric field for charge collection, thus increase the magnitude of the electron-hole recombination. A method usually employed for reducing the pulse height defect caused by this is to increase the bias voltage. However, the leakage current, which will be increased by the radiation damage described in the next section, may limit the maximum bias voltage and make this method impractical. The recombination effect is expected to depend also on the relative orientation of the particle path with respect to the electric field. Therefore, in the present experiment, the energy resolution has been measured for inclined particle injection as well as normal injection with respect to the Ge crystal (Fig. 2.8).

### 1.3.5 Radiation Damage

Incident particles collide with lattice atoms and knock them out of their normal positions with a certain probability. The resulting structural defects cause imperfection of charge collection because they capture charge carriers in the semiconductors. Therefore after long irradiation, the degradation of energy resolution appears. A review of the radiation damage of Ge detector for protons can be found in Ref. [10]. According to this review, Ge detectors lose their resolution after irradiation of  $\sim 10^9$  protons/cm<sup>2</sup>, which corresponds to 10 days use at a rate of 1 kcps. It is also reported that, in the case of Si detectors, the effect of radiation damage by heavy ions is remarkable compared with that by light ions [11]. Thus, Ge detectors must be carefully protected against heavy particle radiations.

# Chapter 2

## Experimental Arrangement

Table 2.1 summarizes the measurements discussed in this thesis. All the experiments were performed in the E4 experimental area at RIKEN Accelerator Research Facility (RARF). The schematic layout of RARF is shown in Fig. 2.1.

Table 2.1: List of the experiments.

Date	Beam	Energy	Measurement
Nov. 16, 2002	$^{14}\text{N}$	135 MeV/A	Energy resolution of HPGe
Jun. 26, 2003	$^{40}\text{Ar}$	95 MeV/A	Emittance for various injection phase
Oct. 21, 2003	$^{22}\text{Ne}$	110 MeV/A	Emittance for multi-turn extraction

The test of HPGe detector was carried out using the  $^{14}\text{N}$  beam from the RRC in November, 2002. Though our interest is to estimate energy resolution of HPGe for particles with energy around 60 MeV/A, which is the injection energy in RIBF, the highest beam energy 135 MeV/A was chosen in order to reduce contributions from energy-loss straggling. The  $^{14}\text{N}$  beam accelerated by the AVF cyclotron and the RRC was transported to a scattering chamber in the E4 experimental area and elastically scattered by a gold target. Scattered particles were momentum-analyzed by the magnetic spectrometer SMART (Sec. 2.5) [12] and detected at the second focal plane by a HPGe detector (EURISYS MEASURES: EGM 3800-30-R) with an active slit for defining the momentum.

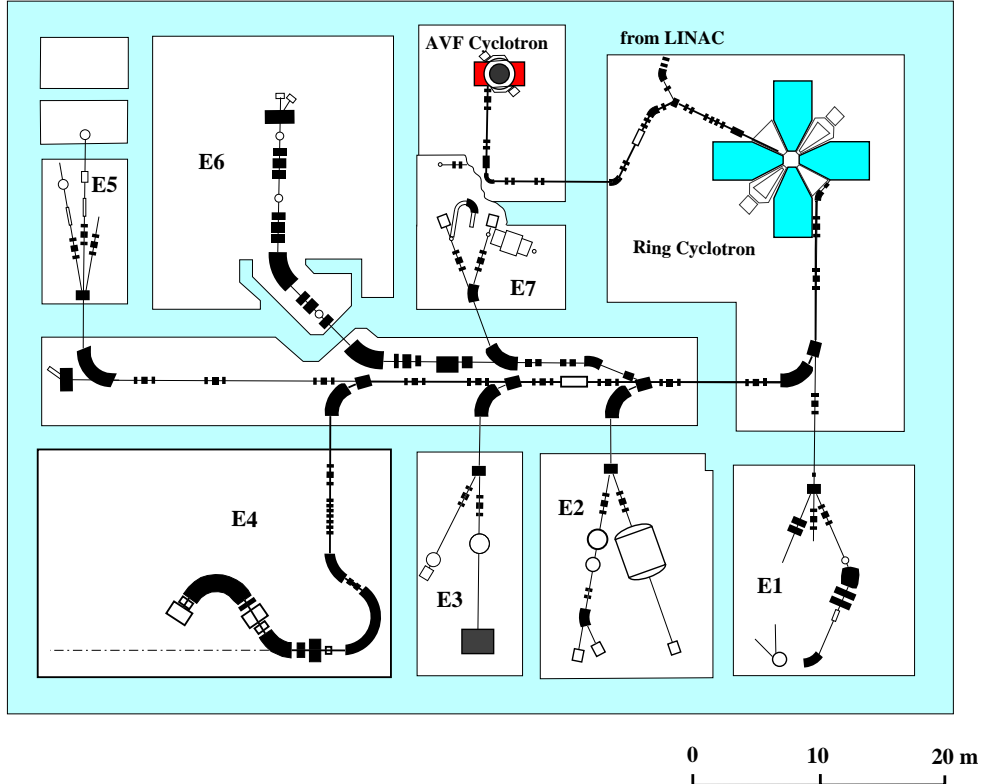


Figure 2.1: Schematic layout of RIKEN Accelerator Research Facility.

The longitudinal emittances of  $^{40}\text{Ar}$  at 95 MeV/ $A$  and  $^{22}\text{Ne}$  at 110 MeV/ $A$  from the RRC were measured also utilizing the spectrometer in June and October, 2003, respectively. After scattered by a gold target and momentum-analyzed, particles were detected at the second focal plane by a pair of plastic scintillation counters followed by a silicon position-sensitive detector. In the study of  $^{40}\text{Ar}$ , the injection time of the beam to the RRC was displaced with respect to RF phase to cover the wide range of beam distribution (see Fig. 1.7). Voltages applied to Dees of the RRC were also varied for the same purpose in the measurement of  $^{22}\text{Ne}$  beam emittance.

## 2.1 AVF Cyclotron

The AVF cyclotron has  $K = 70$  MeV. It consists of four spiral sectors and two Dees with an angle of  $85^\circ$  (Fig. 1.3). The pole diameter is 1.73 m and the gap between

the poles is 300 mm. The maximum flux density is 1.7 Tesla. The mean extraction radius is 714 mm, which is the four-fifth of the mean injection radius of the RRC. RF is tunable from 12 to 24 MHz, which corresponds to the accelerating energy from 3.8 to 14.5 MeV/ $A$  for ions having a mass to charge ratio smaller than 4. The harmonic number  $h_{AVF}$  is 2. To improve the extraction efficiency and beam quality, a flat-top acceleration system was installed in collaboration with the Center for Nuclear Study (CNS), Graduate School of Science, University of Tokyo, in 2001 [13] and has been used in routine operations. The flat-top acceleration voltage is generated by a superposition of the fundamental frequency (12–24 MHz) and 3rd-harmonic (36–72 MHz) frequency. This system reduces the momentum and time spreads of the beam and improves the transmission, not only for the AVF but also for the RRC.

## 2.2 Ring Cyclotron

The RRC has  $K = 540$  MeV. It consists of four sectors with an angle of  $50^\circ$  and two Dees with an angle of  $23.5^\circ$  (Fig. 1.3). The pole gap is 80 mm and the maximum flux density is 1.67 Tesla. The beam pre-accelerated by the AVF cyclotron is transported through the beam line 4 m above the median plane of the RRC and levelled down

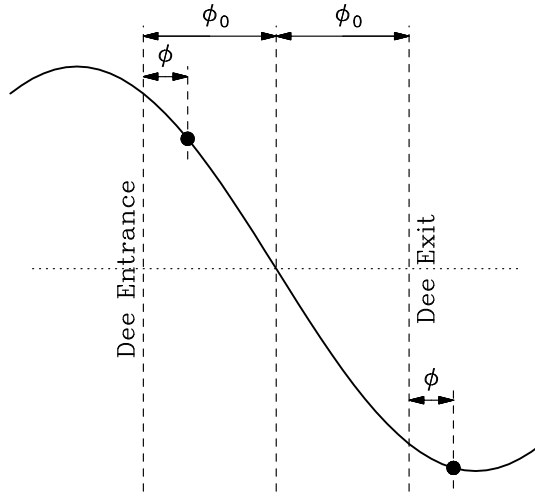


Figure 2.2: Dependence of acceleration voltage on the relative phase  $\phi$ .

into the medium plane at a slope of  $45^\circ$  by a couple of  $45^\circ$  bending magnets, a quadrupole doublets and a quadrupole singlet. Each of Dees can generate 275 kV at maximum. The Dee voltage has a radial distribution for the purpose of phase compression described in Sec. 1.2.6, and  $V_{\text{ext}}/V_{\text{inj}} = 1.6$  for the frequencies operated at the present experiments. RF is tunable from 18 to 45 MHz and the operational RF is twice that of the AVF. The harmonic number  $h_{\text{RRC}}$  is 5 in the case of the AVF injection, thus particles are not accelerated at the highest voltage (Fig. 2.2). However, the quadratic relation in Eq. (1.11) is applied also in this case, because the dependence of acceleration voltage on the relative phase  $\phi$  is expressed as

$$\begin{aligned} V(\phi) &= V_0(\sin(\phi_0 - \phi) + \sin(\phi_0 + \phi)) \\ &= 2V_0 \sin \phi_0 \cos \phi, \end{aligned}$$

where

$$\phi_0 = \frac{23.5^\circ}{2} \times h_{\text{RRC}} \simeq 60^\circ.$$

The injection radius is 0.89 m on the average, while the extraction radius is 3.56 m. The velocity gain is 4, which is equivalent to the ratio of the extraction to injection radii. Since the ratio of the AVF extraction radius to the RRC injection radius is  $4/5$ , while  $h_{\text{AVF}}/h_{\text{RRC}} = 2/5$ , the beam exists only in alternate RF buckets as shown in Fig. 2.3. Thus the beam bunches in neighboring turns are extracted at different times by  $1/f_{\text{rf}}$  (cf. Fig. 4.6). This configuration is useful to diagnose single turn extraction. An example is presented in Sec. 4.3. The beam accelerated up to the extraction radius is peeled off by an EDC and extracted from the RRC through a couple of MDCs. Two bending magnets, EBM1 and EBM2, guide the extracted beam to the transport line. The accelerator parameters of the AVF and the RRC in the present experiments are summarized in Table 2.2.

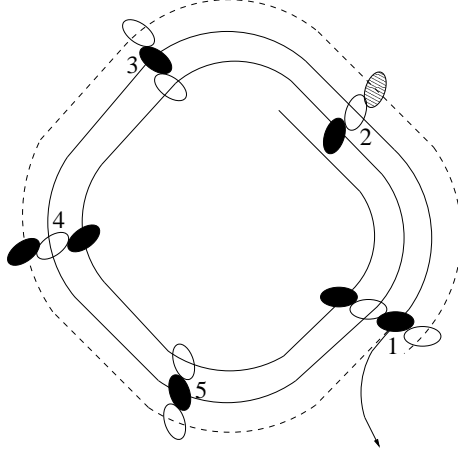


Figure 2.3: Beam configuration in the RRC in the case of the AVF injection.

Table 2.2: Accelerator parameters.

Beam	AVF RF	RRC RF	Harmonics	Intensity
135-MeV/A $^{14}\text{N}^{7+}$	16.30 MHz	32.6 MHz	5	50 enA
95-MeV/A $^{40}\text{Ar}^{17+}$	14.05 MHz	28.1 MHz	5	50 enA
110-MeV/A $^{22}\text{Ne}^{10+}$	15.05 MHz	30.1 MHz	5	100 enA

## 2.3 Beam Transport

The beam extracted from the RRC is transported to the target in the E4 experimental area through the transport system shown in Fig. 2.4. The transport system consists of six dipoles (EBM1, EBM2, DAA1, DMA1, DAD4, DMD4), nine quadrupole triplets (QA01, QA02, QA11, QD12, QD13, QD14, QD15, QD16, Q4A1), a quadrupole septenary (TWISTER), a set of two dipoles (WD1, WD2) and a quadrupole doublet (WQ1, WQ2). The TWISTER, WD1, WD2, WQ1 and WQ2 are the parts of the spectrometer SMART described later. A removable charge stripping foil (STRIP in Fig. 2.4) can be inserted between QA01 and QA02. This foil was used for the purpose of measuring the dependence of time-of-flight on the momentum of the beam in the experiment using the  $^{22}\text{Ne}$  beam. Details are described later in Sec. 3.5.

A typical beam envelope calculated by using the computer code TRANSPORT [14] is shown in Fig. 2.5. The transfer matrix from the EDC to the target is

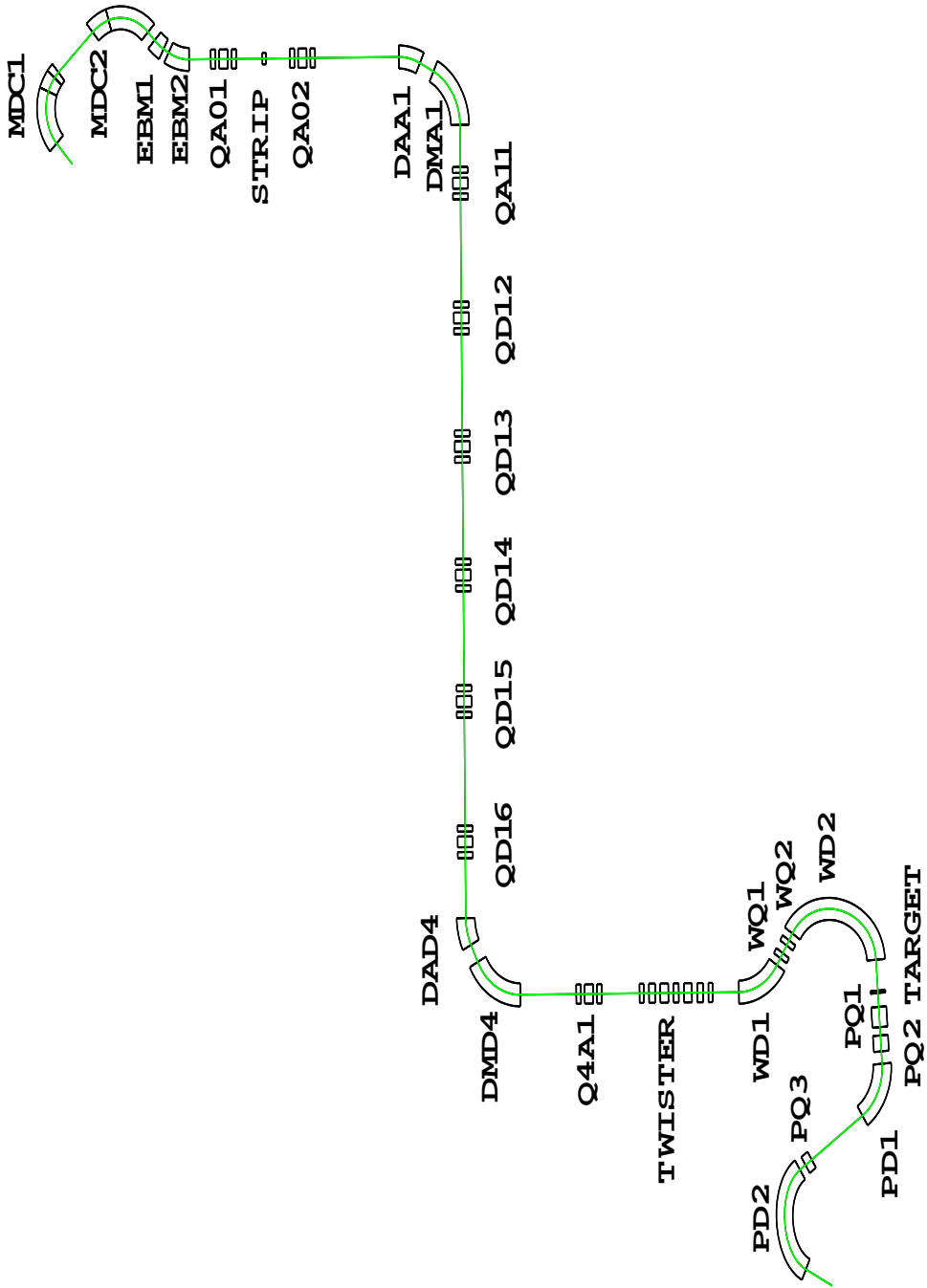


Figure 2.4: Transport line components from the RRC to F2 of SMART together with the extraction components of the RRC.

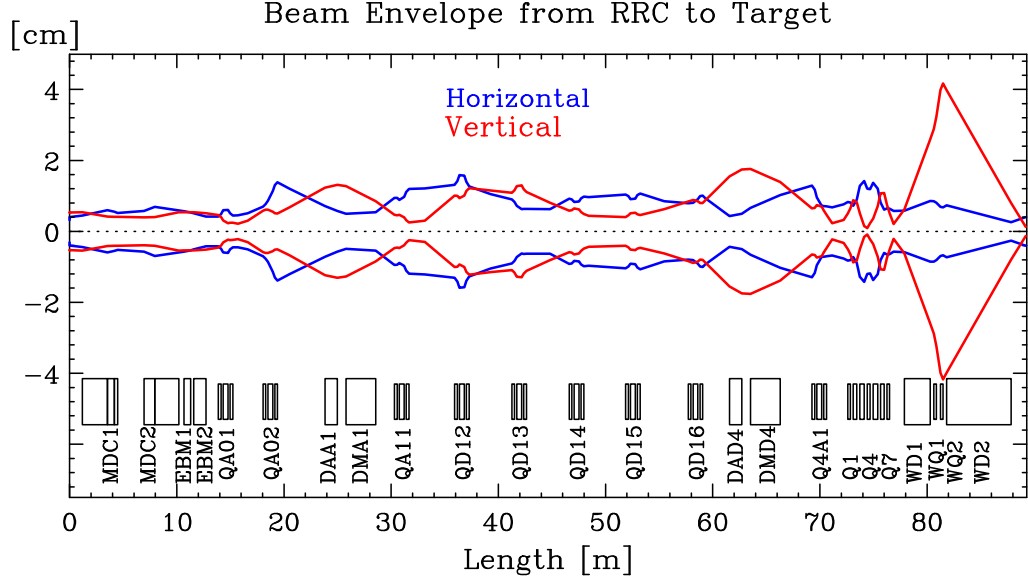


Figure 2.5: A Typical beam envelope from the RRC to the target of scattering chamber in E4 experimental area.

$$\begin{bmatrix} x' \\ a' \\ y' \\ b' \\ l' \\ \delta' \end{bmatrix} = \begin{bmatrix} 0.8089 & -0.0430 & 0 & 0 & 0 & -3.1035 \\ 18.857 & 1.9009 & 0 & 0 & 0 & -22.837 \\ 0 & 0 & -0.1378 & -0.1151 & 0 & 0 \\ 0 & 0 & 9.7494 & 0.8878 & 0 & 0 \\ -0.2214 & -0.8719 & 0 & 0 & 1 & -7.7312 \\ 0 & 0 & 0 & 0 & 0 & 1 \end{bmatrix} \begin{bmatrix} x \\ a \\ y \\ b \\ l \\ \delta \end{bmatrix}, \quad (2.1)$$

where  $x$  and  $y$  denote horizontal and vertical positions in cm,  $a$  and  $b$  horizontal and vertical angles in mrad, and  $\delta = \delta p/p$  in %, respectively.

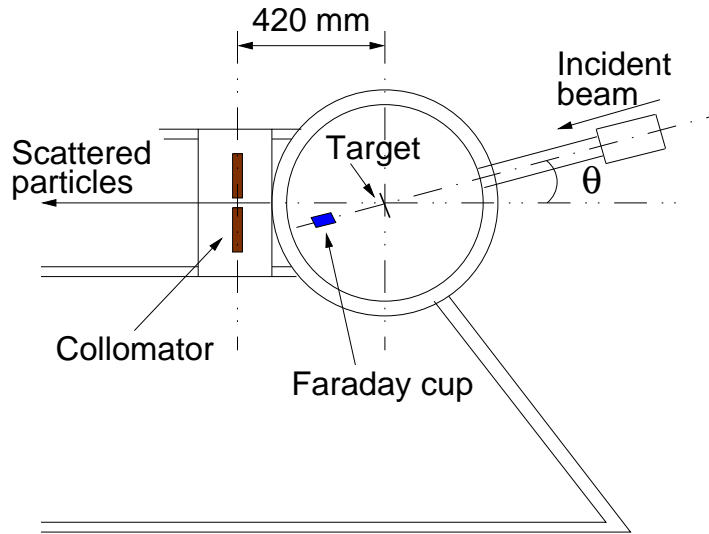


Figure 2.6: Side view of the SMART scattering chamber.

## 2.4 Target and Collimator

Figure 2.6 shows a schematic view of the scattering chamber. It is a cylindrical chamber with an inner diameter of 510 mm and equipped with a turning table. Since the beam injection angle is rotated by the beam swinger system described in the next section, the Faraday cup is installed on the turning table. The target is rotated so that the thickness viewed by the incident beam is kept constant. To keep the count rate of detectors reasonable, elastically scattered particles are measured instead of direct measurement of the beam. The scattering angle  $\theta$  must be sufficiently small in order to obtain a good signal-to-noise ratio (elastic to non-elastic scattering ratio), but can not be  $\sim 0^\circ$  to separate scattered particles from the beam. In the present experiments,  $\theta = 2^\circ$  was chosen (cf. Fig. A.1). Usually the beam on target has a distribution with width of a few mm. To make the most of the momentum resolving power of the SMART, a gold strip target with 1-mm width and 1- $\mu\text{m}$  thickness was used in the energy resolution measurement of HPGe, while an ordinary gold foil target with 0.25- $\mu\text{m}$  thickness was used in the longitudinal emittance measurements in order to reduce the energy-loss straggling.

To keep the higher order effects other than  $(x|\delta)$  small, a 5.5-mm thick tantalum collimator with an aperture of 5 mm in diameter was set 420-mm downstream from the target, which corresponds to the 12-mrad angular acceptance. Due to the finite mass of the target, the angular acceptance also contributes to the energy spread. The energy dependence on the scattering angle  $dE/d\theta$  and the energy spread  $\Delta E_{\text{ang}}$  due to the angular acceptance of the collimator are calculated according to the two-body kinematics and summarized in Table 2.3. Also the energy spread  $\Delta E_{\text{straggle}}$  due to the energy-loss straggling in the target, together with target thickness, and their quadratic sum  $\Delta E_{\text{total}}$  are presented. They are comparable to the resolution of SMART and sufficiently smaller than the beam energy spread.

Table 2.3: Energy spreads due to the angular acceptance of the collimator  $\Delta E_{\text{ang}}$  and the energy-loss straggling in the target  $\Delta E_{\text{straggle}}$  (FWHM).

	$^{14}\text{N}$	$^{22}\text{Ne}$	$^{40}\text{Ar}$	units
Beam energy $T$	1890	2420	3800	[MeV]
$dE/d\theta$	10.1	20.0	56.6	[MeV/rad]
$\Delta E_{\text{ang}}$	0.12	0.24	0.68	[MeV]
Target thickness	1	0.25	0.25	[ $\mu\text{m}$ ]
$\Delta E_{\text{straggle}}$	0.13	0.09	0.16	[MeV]
$\Delta E_{\text{total}}$	0.18	0.33	0.84	[MeV]
$\Delta E_{\text{total}}/T$	0.95	1.36	2.21	$\times 10^{-4}$

## 2.5 Magnetic Spectrometer SMART

The magnetic spectrometer SMART [12] is composed of the beam twister, the beam swinger, and the magnetic analyzer consisting of QQD-QD magnet series (Fig. 2.7). Different from ordinary spectrometer systems, the scattering angle is changed by rotating the beam swinger while the analyzer is fixed on the ground. The twister is used to keep the beam emittance irrespective of the scattering angle. The analyzer has two focal planes, F1 and F2, each of which serves as the large-acceptance and high-

resolution spectrometer, respectively. The typical optics properties of the SMART are summarized in Table 2.4.

The first order transfer matrix from the target to F2 calculated by using RAYTRACE is

$$\begin{bmatrix} x' \\ a' \\ y' \\ b' \\ \delta' \end{bmatrix} = \begin{bmatrix} 0.5212 & -0.0007 & 0 & 0 & -7.5131 \\ 18.8574 & 1.9009 & 0 & 0 & -38.0819 \\ 0 & 0 & -0.8337 & -0.0578 & 0 \\ 0 & 0 & 16.078 & -0.0946 & 0 \\ 0 & 0 & 0 & 0 & 1 \end{bmatrix} \begin{bmatrix} x \\ a \\ y \\ b \\ \delta \end{bmatrix}, \quad (2.2)$$

where  $x$  and  $y$  denote horizontal and vertical positions in cm,  $a$  and  $b$  horizontal and vertical angles in mrad, and  $\delta = \delta p/p$  in %, respectively. The momentum resolution in Table 2.4 is calculated by assuming a beam width of 1 mm on the target. The most important matrix element in Eq. (2.2) is  $(x|\delta)$ , which is experimentally determined to be  $-7.7$  cm/% in the present experiments. Other terms, including higher order matrix elements, have negligible contributions due to the small acceptance of the collimator.

Table 2.4: Typical optical characteristics of the SMART.

Focal plane	F1	F2
Magnet arrangement	Q-Q-D	Q-Q-D-Q-D
Momentum dispersion	3.4 m	7.5 m
Momentum resolution $p/\delta p$	3000	13000
Momentum acceptance $\Delta p/p$	15 %	4%
Angular acceptance	20 msr	10 msr

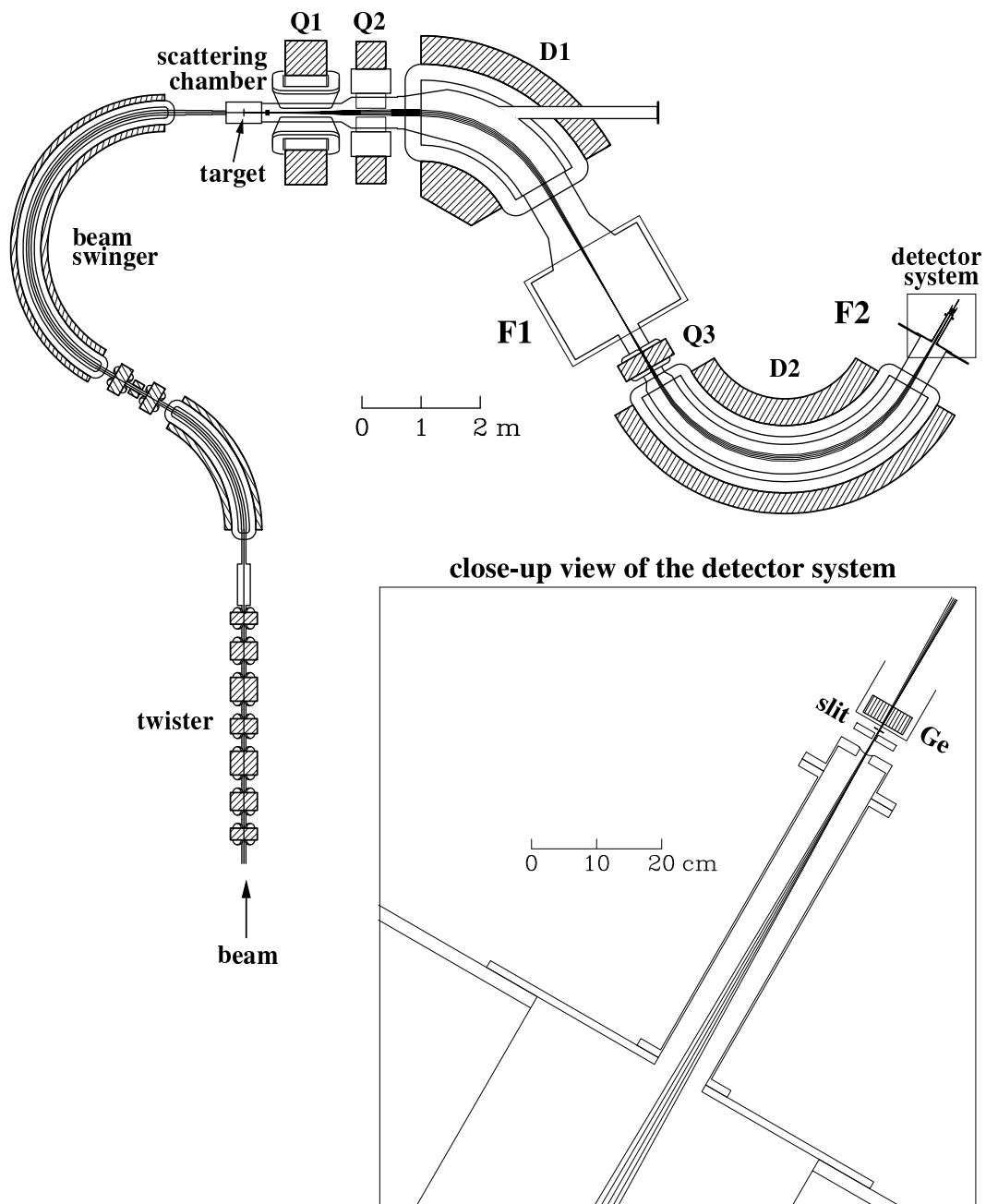


Figure 2.7: Arrangement of SMART and the detector system.

## 2.6 Detector Systems

Two types of detector systems were used for the present experiments: (1) the system for the energy resolution measurement, composed of a HPGe detector and brass and scintillator active slits, which are used for defining the particle momentum as shown in Fig. 2.8, and (2) the system for the longitudinal emittance measurements, composed of a silicon position sensitive detector (Si-PSD) and a pair of plastic scintillators detecting the position and timing of particles, respectively (Fig. 2.9).

### 2.6.1 Energy Resolution Measurement

In the energy resolution measurement, momentum-analyzed particles were brought to the atmosphere through a  $16\text{-}\mu\text{m}$  aramid window, collimated by the slits and detected by the HPGe detector. The brass slit with a thickness of 10 mm was set 20-mm downstream from the vacuum window to protect HPGe against undesirable irradiation. The aperture size was  $3\text{ mm}^{\text{W}} \times 12\text{ mm}^{\text{H}}$ . Behind the brass slit, the active slit made of plastic scintillator with a thickness of 0.1 mm and an aperture

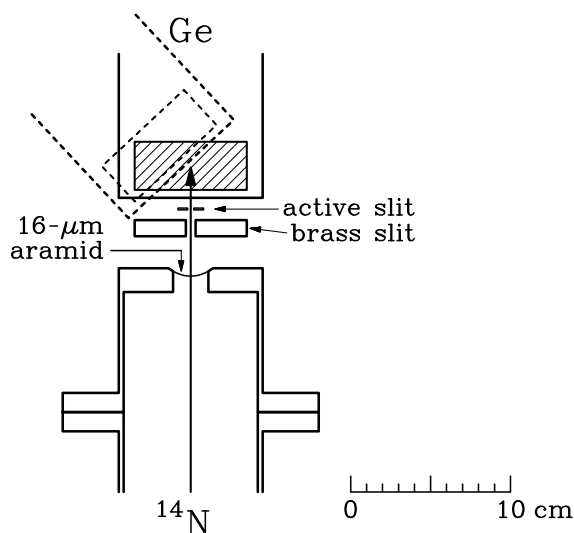


Figure 2.8: Setup of the HPGe detector and the slits for the energy resolution measurement.

of  $1 \text{ mm}^{\text{W}} \times 10 \text{ mm}^{\text{H}}$  was located. According to Eq. (2.2), the 1-mm aperture width corresponds to a relative momentum width of  $1.3 \times 10^{-4}$ . The active slit was attached to a photo multiplier tube (PMT) via a light guide. A carbon aramid foil with a thickness of  $9 \text{ }\mu\text{m}$  was used for light shield. Using the active slit, particles scattered from the edge of the brass slit were vetoed, which, otherwise, cause a tail of peak in the spectrum.

The HPGe detector (EURISYS MEASURES: EGM 3800-30-R) consisted of a Be entrance window of  $300\text{-}\mu\text{m}$  thickness and a semi-planar HPGe crystal with 30-mm thickness and 70-mm sensitive diameter. The crystal was mounted 5-mm behind from the entrance window in a cryostat. This detector was specially fabricated for the measurement of intermediate energy protons by Kobayashi group at Tohoku University and was kindly loaned to us for this experiment. Although the feedback capacitor of the preamplifier was modified to allow the measurement up to  $\sim 4\text{-GeV}$  particles, the thick Be window is not appropriate for heavy ion detection and must be carefully treated in the analysis. Also the HPGe detector was set either perpendicular or inclining by  $43^\circ$  to the particle path (Fig. 2.8), expecting to see the influence of the electric field direction on the charge collection, which may be deteriorated by the high density of electron-hole pairs as described in Sec. 1.3.4. The difference of energy-loss straggling in the air between the vacuum window and the detector, 44 mm and 65 mm for normal and inclined injections, respectively, must be taken into consideration in the analysis. The detector was operated at the liquid nitrogen temperature with a bias voltage of  $-4000 \text{ V}$ .

## 2.6.2 Longitudinal Emittance Measurements

In the longitudinal emittance measurements, momentum-analyzed particles were brought to the atmosphere through a  $50\text{-}\mu\text{m}$  Kapton vacuum window (See Fig. 2.9). Two plastic scintillators,  $J1$  (front) and  $J2$  (rear), measured the arrival time of the particles.

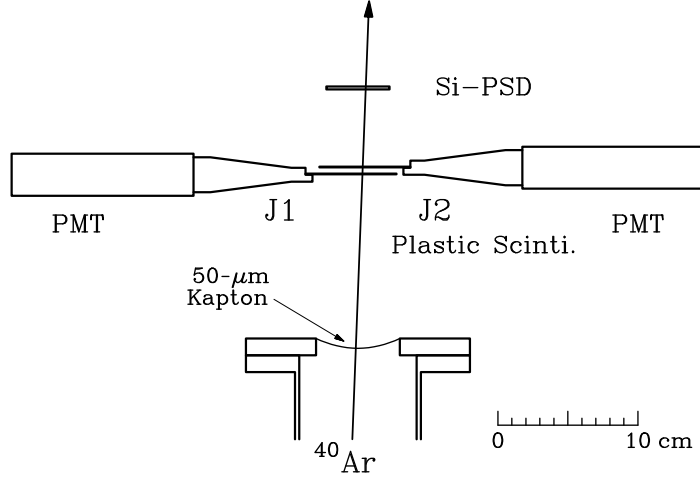


Figure 2.9: Setup of Si-PSD and the plastic scintillators for the longitudinal emittance measurements.

They have sensitive areas of  $65 \text{ mm} \times 55 \text{ mm}$  and a thickness of  $0.5 \text{ mm}$ . The PMTs were shielded by iron tubes in order to prevent the reduction of signals due to stray field produced by the second dipole magnet of the spectrometer. Since the PMT and the light guide were attached to the opposite side for each scintillator, the averaged time

$$t_{\text{av}} = \frac{t_{J1} + t_{J2}}{2}$$

becomes almost position-independent. The time resolution, on the other hand, is estimated from the spread of time difference between  $J1$  and  $J2$ ,

$$t_{\text{diff}} = t_{J1} - t_{J2}.$$

After correcting the position dependence,  $\delta t_{\text{diff}} = 212$  and  $218 \text{ ps}$  (FWHM) have been obtained from the data of  $3800\text{-MeV } ^{40}\text{Ar}$  and  $2420\text{-MeV } ^{22}\text{Ne}$ , respectively. By assuming  $\delta t_{J1} = \delta t_{J2}$ ,  $\delta t_{\text{av}}$  is related to  $\delta t_{\text{diff}}$  as

$$\delta t_{\text{av}} = \frac{\sqrt{\delta t_{J1}^2 + \delta t_{J2}^2}}{2} = \frac{\delta t_{\text{diff}}}{2},$$

which results in 106 and 109 ps (FWHM) for  $^{40}\text{Ar}$  and  $^{22}\text{Ne}$ , respectively.

A silicon position sensitive detector (Si-PSD), Hamamatsu S2461, was used to measure the horizontal positions of the particles at F2. The Si-PSD is a strip detector consisting of 48 p-type silicon strips and an n-type silicon base with 250- $\mu\text{m}$  thickness. Each strip is 48 mm in length and 0.9 mm in width and implanted on the silicon base at intervals of 1 mm. An aluminum electrode is mounted on each strip and connected to an external resistive divider network system giving discrete readouts. A simplified equivalent circuit along with the layout of the strips is shown in Fig. 2.10. The operating voltage of  $-60$  V was applied to the Si-PSD in order to obtain full depletion. Two output signals from Si-PSD,  $Q_{\text{left}}$  and  $Q_{\text{right}}$ , can be expressed as

$$Q_{\text{left}} = Q \frac{r_1 + R \frac{x}{L}}{r_1 + r_2 + R} \quad (2.3)$$

$$Q_{\text{right}} = Q \frac{r_2 + R \frac{L-x}{L}}{r_1 + r_2 + R},$$

where  $L$  is the length of Si-PSD,  $Q$  is the charge produced by an incident particle injected at the distance  $x$  from the left end of the range,  $R$  is an impedance of the circuit of Si-PSD and  $r_1$  and  $r_2$  are input impedances of preamplifiers. Equation (2.3)

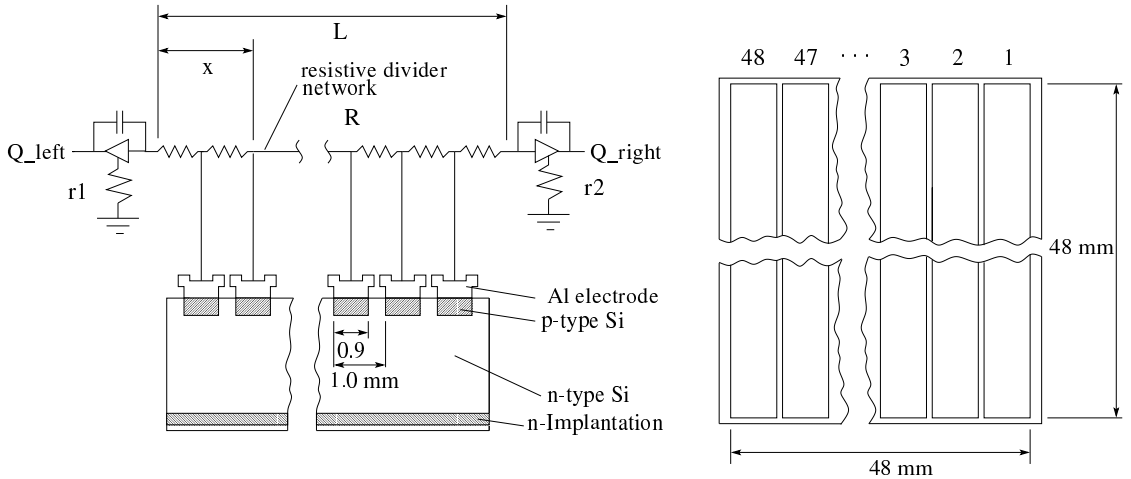


Figure 2.10: A simplified equivalent circuit and the layout of Si-PSD.

can be written as

$$\begin{aligned} Q_{\text{left}} &= Ax + B \\ Q_{\text{right}} &= A(L-x) + C . \end{aligned} \tag{2.4}$$

The parameters  $B$  and  $C$  are obtained by using a pulse generator and a dedicated calibrator (See sec.3.4.). Then the position  $x$  is given by

$$x = \frac{Q_{\text{left}} - B}{(Q_{\text{left}} - B) + (Q_{\text{right}} - C)} L . \tag{2.5}$$

## 2.7 Data Acquisition

A schematic diagram of the data acquisition systems for the energy resolution measurement and the longitudinal emittance measurements are shown in Figs. 2.11 and 2.12, respectively. In the case of the energy resolution measurement, data were stored in HSM (CES High Speed Memory 8170) via FERA bus and FERA driver (LeCroy 4301). In the case of the longitudinal emittance measurements, on the other hand, data were read via CAMAC at each event without buffering. In both cases, data were stored and analyzed on a personal computer running a free-Unix clone, Linux. Details of the data acquisition system can be found in Ref. [15].

### 2.7.1 Energy Resolution Measurement

The signal from HPGe detector was fed to a spectroscopy amplifier (ORTEC 671) and formed to a Gaussian with shaping time of 6  $\mu\text{sec}$ . The unipolar output (UNI in Fig. 2.11) has a pulse height in proportion to the energy deposited in the HPGe. It was digitized by an ORTEC AD413A analog-to-digital converter (ADC) with a 13-bit resolution and subsequently fed to HSM to make energy spectra. The bipolar output (BI) was used for monitoring signals. The logic signal output, counter & rate meter

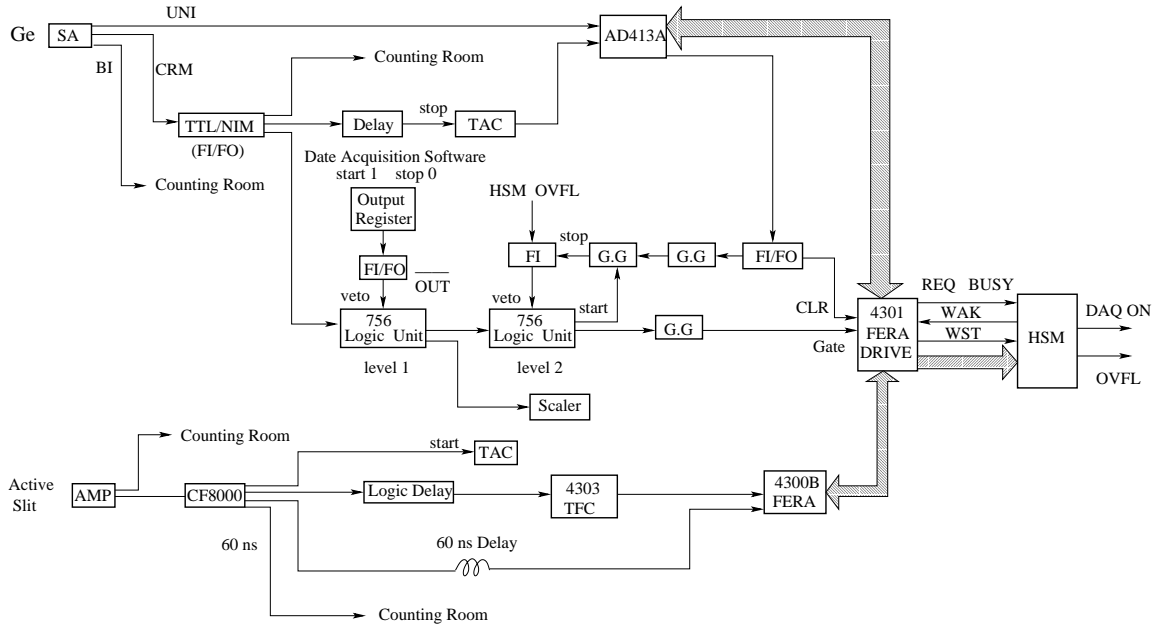


Figure 2.11: Data acquisition system for the energy resolution measurement.

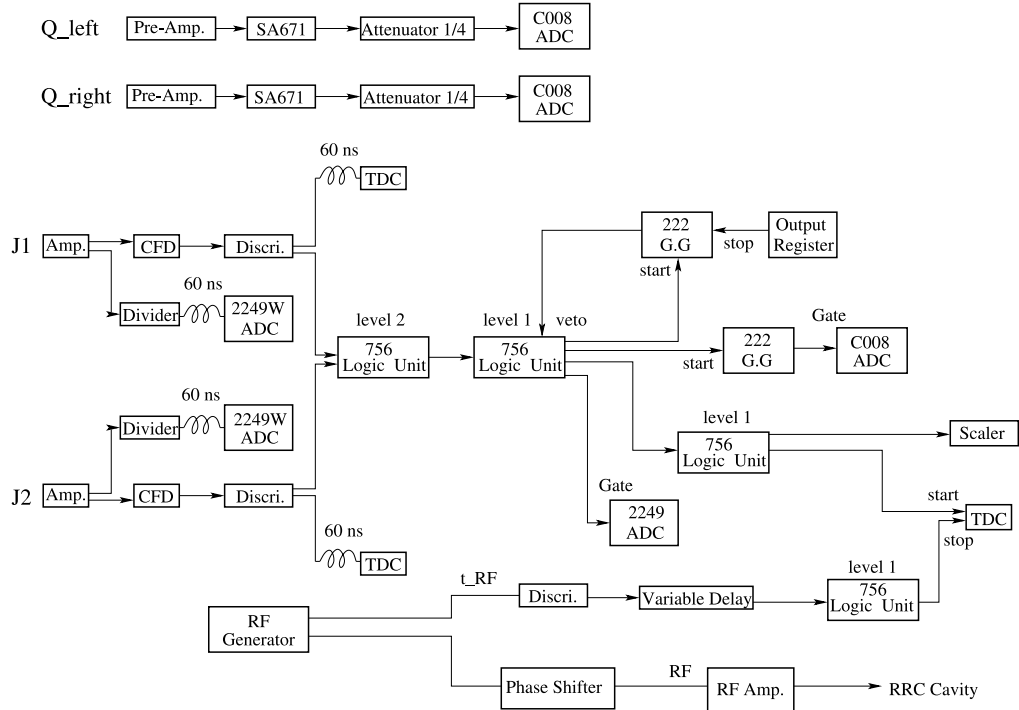


Figure 2.12: Data acquisition system for the longitudinal emittance measurements.

(CRM), was fed to a logic unit (Phillips Scientific 756) and a gate generator (LeCroy 222) to make the gate for ADC. The signal from the active slit was amplified by 10, discriminated by a constant-fraction discriminator (ORTEC CF8000) and fed to an ORTEC 567 time-to-amplitude converter (TAC). The TAC output was converted by AD413A and used for a veto.

### 2.7.2 Longitudinal Emittance Measurements

The signals from plastic scintillators,  $J1$  and  $J2$ , were amplified by Phillips Scientific 776 and fed to a constant fraction discriminator (CFD), Tennelec 454, in the experimental area. The CFD outputs were transmitted to the counting room and discriminated again by a discriminator (LeCroy 821). The outputs were subsequently sent to a time-to-digital converter (TDC), KAIZU 3781A, in order to obtain the information of particle arrival time. The outputs from the discriminator were also used to make a coincidence signal between  $J1$  and  $J2$ , which triggered the data acquisition. The signals from  $J1$  and  $J2$  were also sent to an ADC (LeCroy 2449W). The Si-PSD signals,  $Q_{\text{left}}$  and  $Q_{\text{right}}$ , were transmitted to shaping amplifiers (ORTEC 671) via a preamplifier and subsequently fed to an ADC (HOSHIN C008). It should be noted that the RF signal fed to TDC represents the injection phase and is different from the one fed to the RRC cavities, the phase of which is shifted by a phase shifter (Fig. 2.12).

# Chapter 3

## Analysis

### 3.1 Energy Calibration of HPGe

The output of HPGe was calibrated by using the standard  $\gamma$ -sources,  $^{60}\text{Co}$ ,  $^{22}\text{Na}$  and  $^{137}\text{Cs}$ . Figure 3.1 shows the energy spectra for these sources. The background  $\gamma$  ray from  $^{40}\text{K}$ , as seen in Fig. 3.1, was also used for calibration. The energies of gamma rays and corresponding ADC channels are listed in Table 3.1. The regression line obtained by the least squares method is

$$\text{Energy [keV]} = -4.03 + 0.923 \times \text{ADC [channel]}. \quad (3.1)$$

The energy resolution at 1332.5-keV was 14.2 keV (FWHM) in this calibration. This is reasonably good for measuring energies as large as  $\sim 2$  GeV, although the resolution is generally 2 keV in ordinary  $\gamma$ -ray spectroscopies. The resolution at 1890 MeV is expected to be

$$\frac{\delta E}{E} = \sqrt{\frac{1.333}{1890}} \frac{14.2}{1332.5} = 2.8 \times 10^{-4}$$

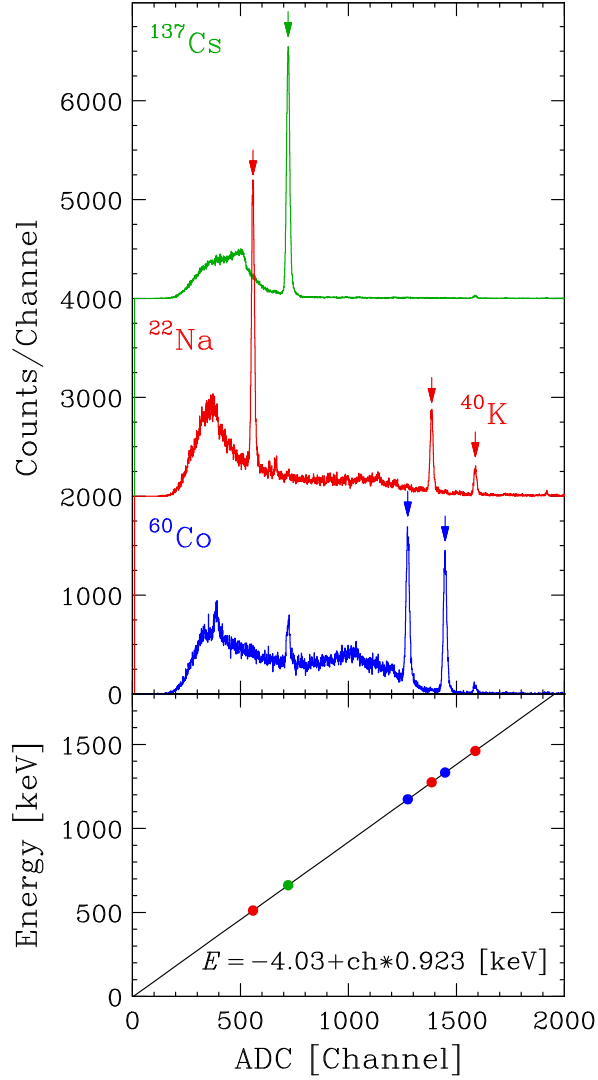


Figure 3.1: Energy spectra from  $^{137}\text{Cs}$ ,  $^{22}\text{Na}$  and  $^{60}\text{Co}$  sources which are used for the energy calibration of ADC channels. The peak from the background,  $^{40}\text{K}$ , was also observed.

if estimated in the same manner as Sec. 1.3.2. The gain of spectroscopy amplifier for the energy resolution measurement was determined to be 4.4 in such a way that 1890 MeV corresponded to 6000 channels, while the gain was 1500 in the  $\gamma$ -ray calibration.

Table 3.1: Energies of  $\gamma$  rays emitted by  $^{60}\text{Co}$ ,  $^{22}\text{Na}$ ,  $^{137}\text{Cs}$  and  $^{40}\text{K}$ , and the corresponding ADC channels.

ADC [channel]	558.4	721.1	1274.9	1385.5	1447.8	1587.8
Energy [keV]	511.0	661.7	1173.3	1274.5	1332.5	1460.9
Source	$^{22}\text{Na}$	$^{137}\text{Cs}$	$^{60}\text{Co}$	$^{22}\text{Na}$	$^{60}\text{Co}$	$^{40}\text{K}$

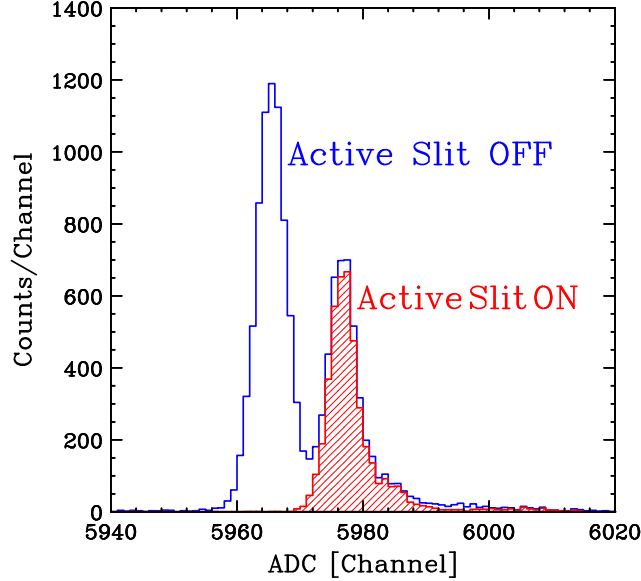


Figure 3.2: Energy spectra for all events (unshaded) and for events without signals from the active slit (shaded).

### 3.2 Veto by Active Slit

Figure 3.2 shows typical energy spectra detected by the HPGe at normal injection. The unshaded one is the spectrum for all events without using the information from the active slit. Two peaks are observed; one at higher energy is formed from particles passing through the 1-mm aperture of active slit, while one at lower energy is from particles which pass through the aperture of brass slit but not the active slit, thus lose some energies in the 0.1-mm scintillator. The shaded one is the spectrum obtained by rejecting events having signals from the active slit. It is clearly seen that the particles penetrating the 0.1-mm scintillator are completely eliminated. The lower energy peak in the unshaded spectrum has a slightly larger width than the one at higher energy, due to the larger aperture of brass slit (3 mm) and the energy-loss straggling in the scintillator, but the difference is not significant because the resolution of HPGe has the largest contribution.

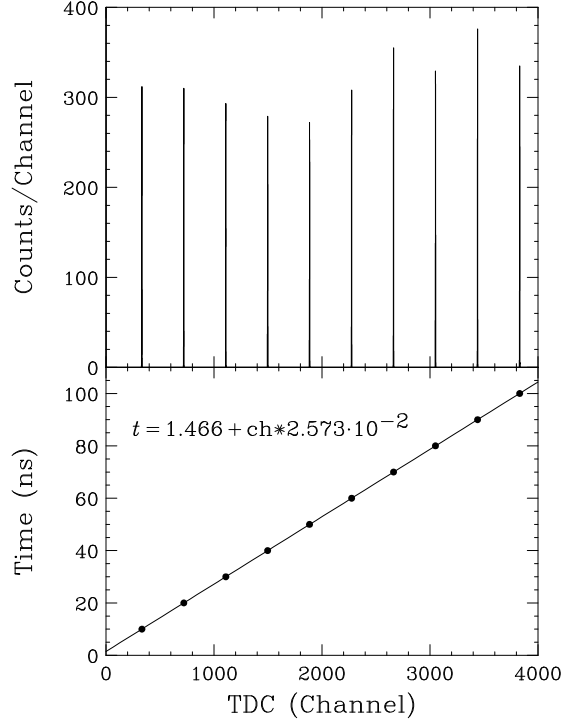


Figure 3.3: Typical time spectrum used for time calibration (upper panel). Pulses from a time calibrator had a 10 ns interval over 100 ns range. The regression line is shown in the lower panel.

### 3.3 Time Calibration

The time calibration was performed by using pulses generated by a time calibrator (ORTEC 462). Each of TDCs reading  $J1$ ,  $J2$  and RF signals was calibrated individually. Figure 3.3 shows one of typical time spectra for pulses having a 10 ns interval over 100 ns range and the regression line obtained by the least squares method.

### 3.4 Position Calibration

Each of ADC channels of Si-PSD signals,  $Q_{\text{left}}$  and  $Q_{\text{right}}$ , was calibrated by using a pulse generator. One of typical spectra and a regression line obtained by the least squares method are shown in Fig. 3.4. Then  $B$  and  $C$  in Eq. (2.5) were determined

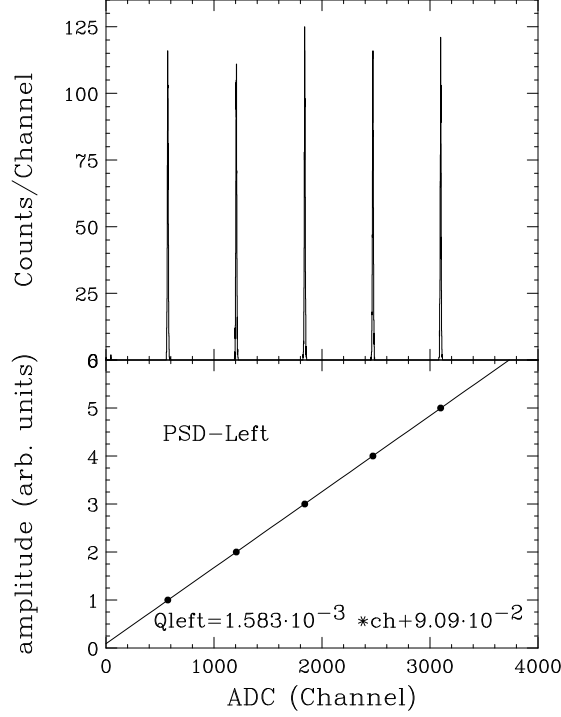


Figure 3.4: Spectrum used for calibration of Left ADC (upper panel). The regression line is shown in the lower panel.

in the following way. Equation (2.4) is reduced to

$$\frac{Q_{\text{left}} - B}{x} = \frac{Q_{\text{right}} - C}{L - x}, \quad (3.2)$$

which is a straight line containing the point  $(B, C)$  in  $(Q_{\text{left}}, Q_{\text{right}})$  plot. Thus  $(B, C)$  is given by the intersecting point of  $Q_{\text{left}}-Q_{\text{right}}$  correlation lines for different  $x$ . These correlation lines were obtained by using a pulse generator and a dedicated position calibrator for Si-PSD. The result is shown in Fig. 3.5. However, Eq. (2.4) is correct only in the ideal case. Since the real detector has stray capacitance, which makes the time constant  $RC$  position-dependent, signals are not linear functions of  $x$  due to the ballistic deficit in shaping circuits. In the present case, fortunately, the discrete structure of the spectrum (Fig. 3.6) definitely gives us information on the absolute position. A third order polynomial giving the correct position  $x$  was determined by the least squares method. In the following analysis, random numbers in  $[0, 1]$  were

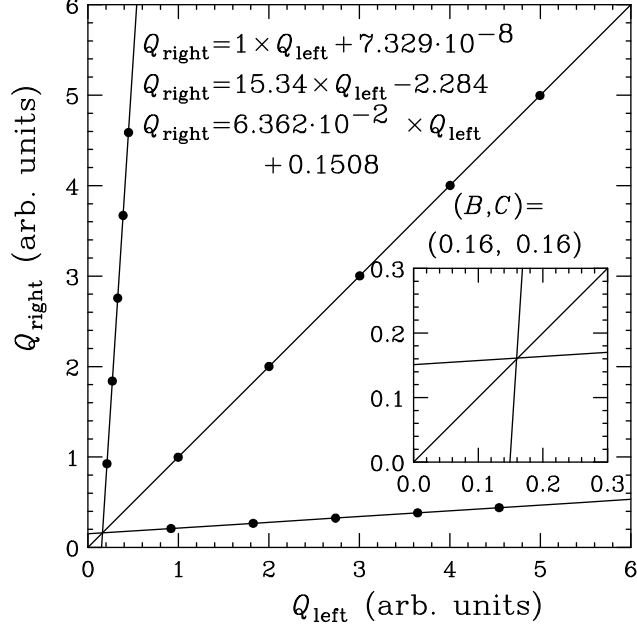


Figure 3.5:  $Q_{\text{left}}-Q_{\text{right}}$  plot for different  $x$  generated by the dedicated position calibrator. The inset is a closeup around the intersecting point.

added to  $x$  for removing spurious structure of the spectra.

### 3.5 Time of Flight Correction

The flight time of particle traveling from the RRC to the detector depends on the particle momentum. This effect must be corrected to obtain the longitudinal emittance of the RRC. The time-of-flight (ToF) is given by

$$t = \frac{L}{v} = \frac{LE}{pc^2},$$

where  $L$  is the flight path length,  $E$  is the total energy and  $p$  is the momentum of a particle. The ToF difference  $\delta t$  is related to the momentum difference  $\delta p$  via

$$\begin{aligned} \delta t &= \left[ \frac{L_0}{c^2} \frac{\partial}{\partial p} \left( \frac{E}{p} \right) + \frac{E_0}{p_0 c^2} \frac{\partial L}{\partial p} \right] \delta p \\ &= \left[ -\frac{1}{\gamma_0^2} + \frac{1}{L_0} \frac{\partial L}{\partial p/p_0} \right] t_0 \frac{\delta p}{p_0}. \end{aligned} \quad (3.3)$$

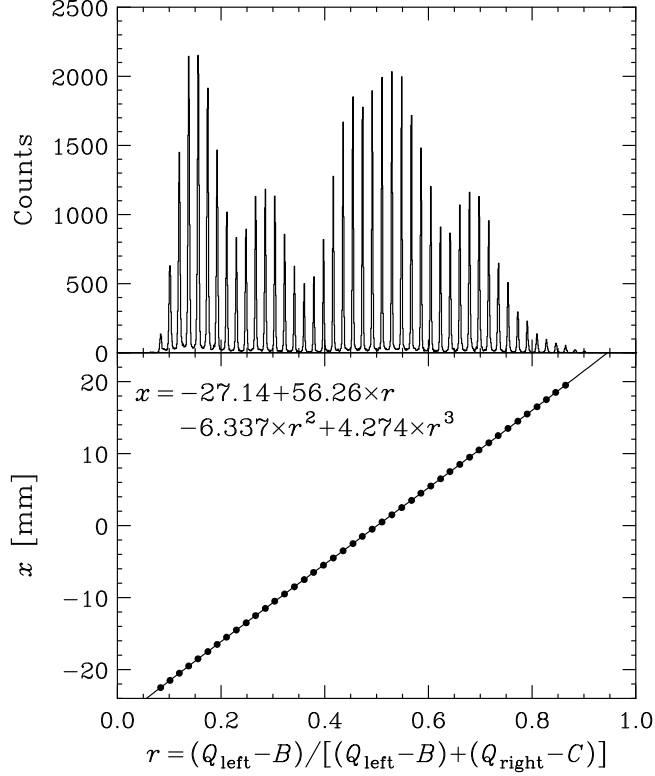


Figure 3.6: Spectrum of  $x/L$  calculated by using Eq. (2.5) (upper panel). Discrete peaks reflecting the strip structure are clearly seen. The lower panel shows the regression curve to deduce the correct position determined by the least squares method.

$L_0$  is the length of the reference orbit. From the first quadrupole of QA02 (Fig. 2.4) to SMART-F2,  $L_0 = 89.5$  m. The transfer matrix element  $\frac{\partial L}{\partial p/p_0} = (l|\delta)$  can be estimated, e.g., by using TRANSPORT, where  $\mathbf{R56} = -(l|\delta)$ . In the code COSY INFINITY [16], even the correction coefficient  $\partial t/(\partial T/T_0)$  is directly given by  $-\text{ME}(5, 6)$ . While the first term in Eq. (3.3) is independent of the transport condition, the second term is very sensitive to the choice of transport parameters and changes even its sign easily. It was determined for each case of  $^{40}\text{Ar}$  and  $^{22}\text{Ne}$  in the following way.

In the case of  $^{40}\text{Ar}$  beam, data were obtained displacing the phase of the RRC Dee voltages relative to the injection phase in step of  $2^\circ$  (198 ps for 28.1-MHz RF). Since the RF signal fed to TDC represents the injection phase (Sec. 2.7.2), the time difference between the RF and the detector does not change if the acceleration is truly isochronous, but it does change due to the phase compression described in Sec. 1.2.6.

According to Eq. (1.13), the shift by the phase compression is proportional to the injection phase with respect to the RF,  $\Delta\phi_{\text{inj}}$ .  $(l|\delta)$  has been artificially determined so as to satisfy this relation. Figure 3.7 shows the time spectra corrected only by the first term in Eq. (3.3). It is seen that time spectra at  $\Delta\phi_{\text{inj}} = +4^\circ$  to  $-2^\circ$  do not shift while time spectra at  $\Delta\phi_{\text{inj}} = -4^\circ$  and  $-6^\circ$  do significantly. On the other hand, by assuming  $(l|\delta) = -35.5 \text{ cm}/\%$ , the corrected time spectra shift approximately in proportion to their injection phases as shown in Fig. 3.8. This hypothetical value is consistent with a transfer matrix element  $(l|\delta) = -32.6 \text{ cm}/\%$  calculated by TRANSPORT. Substituting  $L_0 = 89.5 \text{ m}$  and  $\gamma_0 = 1.1021$  as well as  $(l|\delta) = -35.5 \text{ cm}/\%$  into Eq. (3.3), ToF correction is obtained as

$$\delta t = [-584.8 - 281.7] \frac{\delta p}{p_0} [\text{ns}] . \quad (3.4)$$

In the case of  $^{22}\text{Ne}$  beam, the dependence of ToF on the particle momentum was determined by slightly degrading the momentum with the charge stripper (Fig. 2.4). The shift in  $(t, \delta)$  plot directly gives the coefficient in Eq. (3.3). The used stripper was a carbon foil with a thickness of  $9 \text{ mg}/\text{cm}^2$ . Figure 3.9 shows the correlation spectra,  $h_2(t, \delta)$  and  $h_1(t, \delta)$ , detected at F2 with (right panel) and without the stripper (left panel), respectively. The displacements,  $t_0$  and  $\delta_0$ , were determined so as to minimize the chi squares defined by

$$\chi^2 = \sum_{i,j} [h_1(t_i, \delta_j) - h_2(t_i - t_0, \delta_j - \delta_0)]^2 .$$

The obtained values are  $t_0 = 0.525 \text{ ns}$  and  $\delta_0 = -1.021 \times 10^{-3}$ , resulting in the ToF

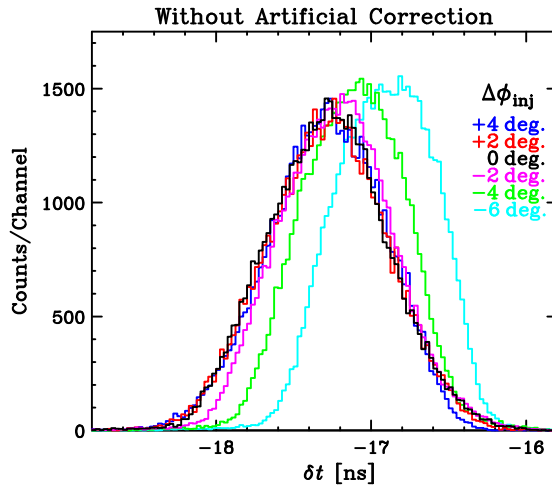


Figure 3.7: Time spectra with the first-term correction only. The injection phase with respect to the RF phase of the RRC,  $\Delta\phi_{\text{inj}}$ , is displaced in step of  $2^\circ$ .

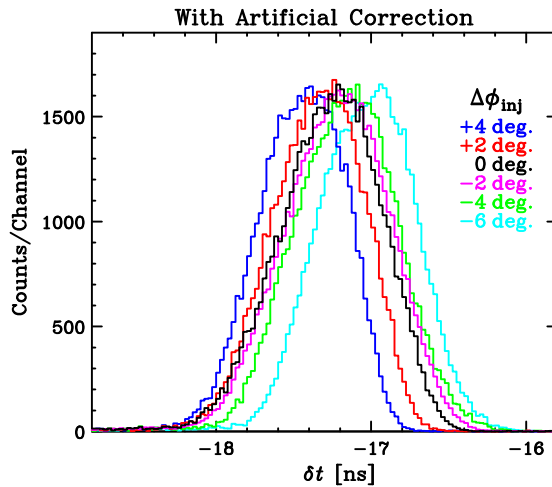


Figure 3.8: Same as Fig. 3.7 but with the correction assuming  $(l|\delta) = -35.5 \text{ cm}/\%$ .

correction to be

$$\delta t = -514.20 \frac{\delta p}{p_0} [\text{ns}] . \quad (3.5)$$

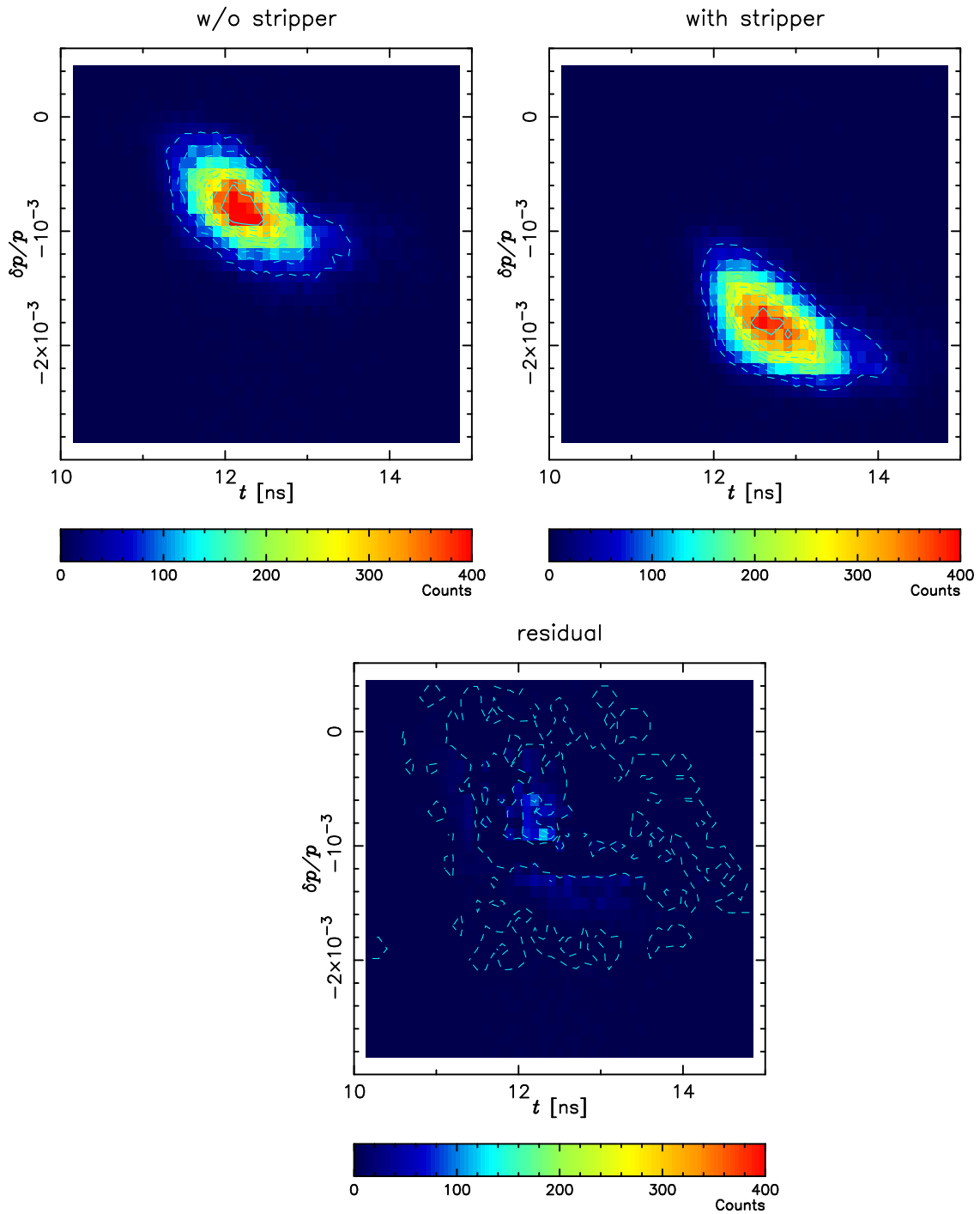


Figure 3.9: The correlation between the time and momentum of particles detected at F2 without the stripper (left) and with the stripper (right).



Figure 3.10: Beam spot on a ZnS scintillation target at the target position with (right panel) and without the stripper foil (left panel). Ticks on the target are marked in 5 mm step.

To justify the above procedure, the beam spot on the target should not move irrespective of the momentum, which is achieved by an achromatic transport. The calculated transfer matrix from the stripper to the target is

$$\begin{bmatrix} x' \\ a' \\ y' \\ b' \\ l' \\ \delta' \end{bmatrix} = \begin{bmatrix} 0.3620 & 0.1745 & 0 & 0 & 0 & 0.8351 \\ -1.5762 & 2.0025 & 0 & 0 & 0 & 4.9694 \\ 0 & 0 & 0.4601 & -0.0785 & 0 & 0 \\ 0 & 0 & -1.1680 & 2.3725 & 0 & 0 \\ -0.3115 & 0.0805 & 0 & 0 & 1 & 1.6120 \\ 0 & 0 & 0 & 0 & 0 & 1 \end{bmatrix} \begin{bmatrix} x \\ a \\ y \\ b \\ l \\ \delta \end{bmatrix}. \quad (3.6)$$

$(x|\delta)$  is not zero but sufficiently small. It was experimentally verified by using a ZnS scintillation target (Fig. 3.10).

# Chapter 4

## Results and Discussions

### 4.1 Energy Resolution of HPGe

Figure 4.1 shows typical energy spectra with the active slit at normal and  $43^\circ$  injections. The peak widths determined by a Gaussian peak fitting are 1.52 MeV and 1.80 MeV (FWHM), which correspond to relative energy spreads of  $\delta E/E = 8.0 \times 10^{-4}$  and  $9.5 \times 10^{-4}$  for the normal and  $43^\circ$  injections, respectively. Subtracting the estimated energy-loss straggling in the  $300\text{-}\mu\text{m}$  Be window and the air between the exit vacuum

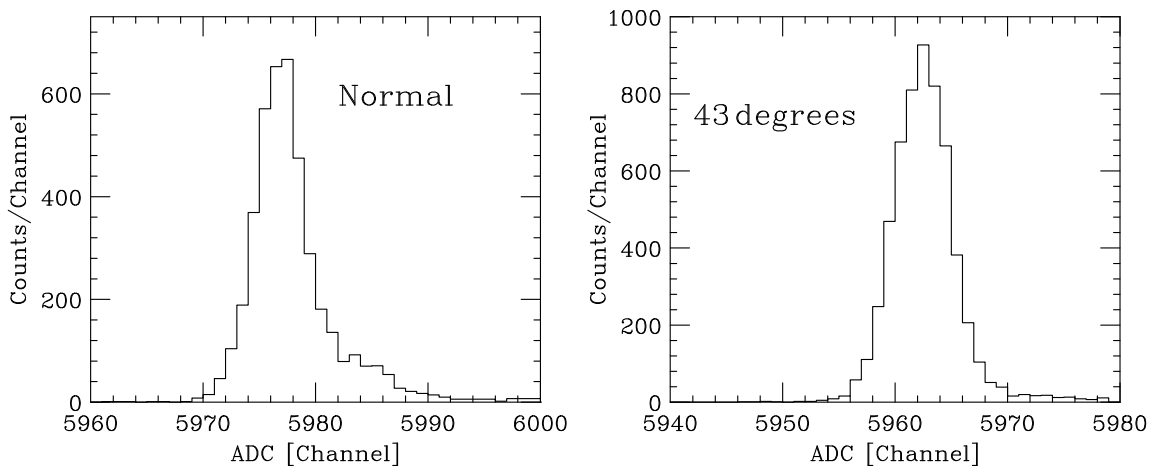


Figure 4.1: Energy spectra with the active slit at normal and  $43^\circ$  injections, respectively.

Table 4.1: Peak width in observed energy spectra, the contributions from energy-loss straggling and the intrinsic energy resolution of HPGe at normal and 43° injections for 1890-MeV  $^{14}\text{N}$ .

Injection Angle	Peak Width	Straggling		Beam Spread	Intrinsic Resolution	Unit
		Be	Air			
Normal	1.52	0.72	0.24	0.47	1.23	MeV
	8.0	3.8	1.3	2.5	6.5	$\times 10^{-4}$
43°	1.80	0.88	0.30	0.47	1.47	MeV
	9.5	4.7	1.6	2.5	7.7	$\times 10^{-4}$

(FWHM)

window and the Be window, the intrinsic energy resolution of HPGe becomes 1.23 MeV and 1.47 MeV (FWHM) for the normal and 43° injections, respectively. The energy-loss straggling in the vacuum window and the light shield is negligibly small. The results are summarized in Table 4.1.

Note that the present HPGe detector is not optimized for our purpose. For example, the use of smaller Ge crystal decreases the leakage current and the capacitance, which results in the lower electronics noise, and allows the use of small and thin Be window, say 25  $\mu\text{m}$ , resulting in the smaller energy-loss straggling. Since the intrinsic resolution achieved in the present experiment is already at a level of practical use, it is concluded that HPGe is promising as an energy detector for longitudinal emittance measurements.

The energy resolution at 43° was slightly worse than that at normal injection, contrary to our expectation that the inclined electric field with respect to the particle path will improve the charge collection, leading to the improvement of energy resolution. There are two possible reasons: One is that, because the HPGe detector was not precisely set on the beam axis (Fig. 2.8), particles were injected near the edge of crystal where the electric field can be weak. A weak electric field deteriorates the charge collection and accordingly the energy resolution. The other is an underestimation of energy-loss straggling in the Be window, which mainly contributes to the

systematic error of energy resolution. This is also suggested even from the data for normal injection, as the observed resolution  $6.5 \times 10^{-4}$  is significantly worse than the one expected from the  $\gamma$ -source data described in Sec. 3.1. The present estimation of energy-loss straggling has some ambiguities since the data in this energy region are rare. The error may be removed by directly measuring the energy-loss straggling in a Be foil with the spectrometer.

## 4.2 Longitudinal Emittance of $^{40}\text{Ar}$ Beam

— case of single turn extraction —

Figure 4.2 shows the longitudinal emittances of 3800-MeV  $^{40}\text{Ar}$ .  $\delta t$  is the extraction time relative to the RF of the RRC, instead of the injection time, and is corrected for ToF according to Eq. (3.4). The injection phase  $\Delta\phi_{\text{inj}}$  is displaced relative to the RF of the RRC in step of  $2^\circ$  (198 ps for 28.1-MHz RF). Like in Fig. 1.7, it is clearly seen that there is a quadratic correlation between  $\delta t$  and  $\delta T/T$ , which is expected from Eq. (1.11). A sinusoidal curve corresponding to the RF of 28.1 MHz is displayed for eye-guide. The correlation is, however, smeared by fairly large spread of distribution. The time and energy spreads are approximately 700 ps and  $1.3 \times 10^{-3}$  (FWHM), respectively. The energy resolution expected from  $(x|\delta)$  of the spectrometer,  $2.5 \times 10^{-4}$ , can be deteriorated by several times due to the beam spread on the target,  $\sim 5$  mm. The time resolution for the scintillators, on the other hand, was confirmed to be 100 ps in the present experiment (Sec. 2.6.2). The other source of time spread is not clear. It is unlikely that the beam in acceleration has such a time spread. The investigation of this spread is critical for the longitudinal emittance measurement. A smaller time spread will be particularly helpful to see the steep correlations more clearly.

Figure 4.2 includes not only the sinusoidal correlation but also the effect of phase

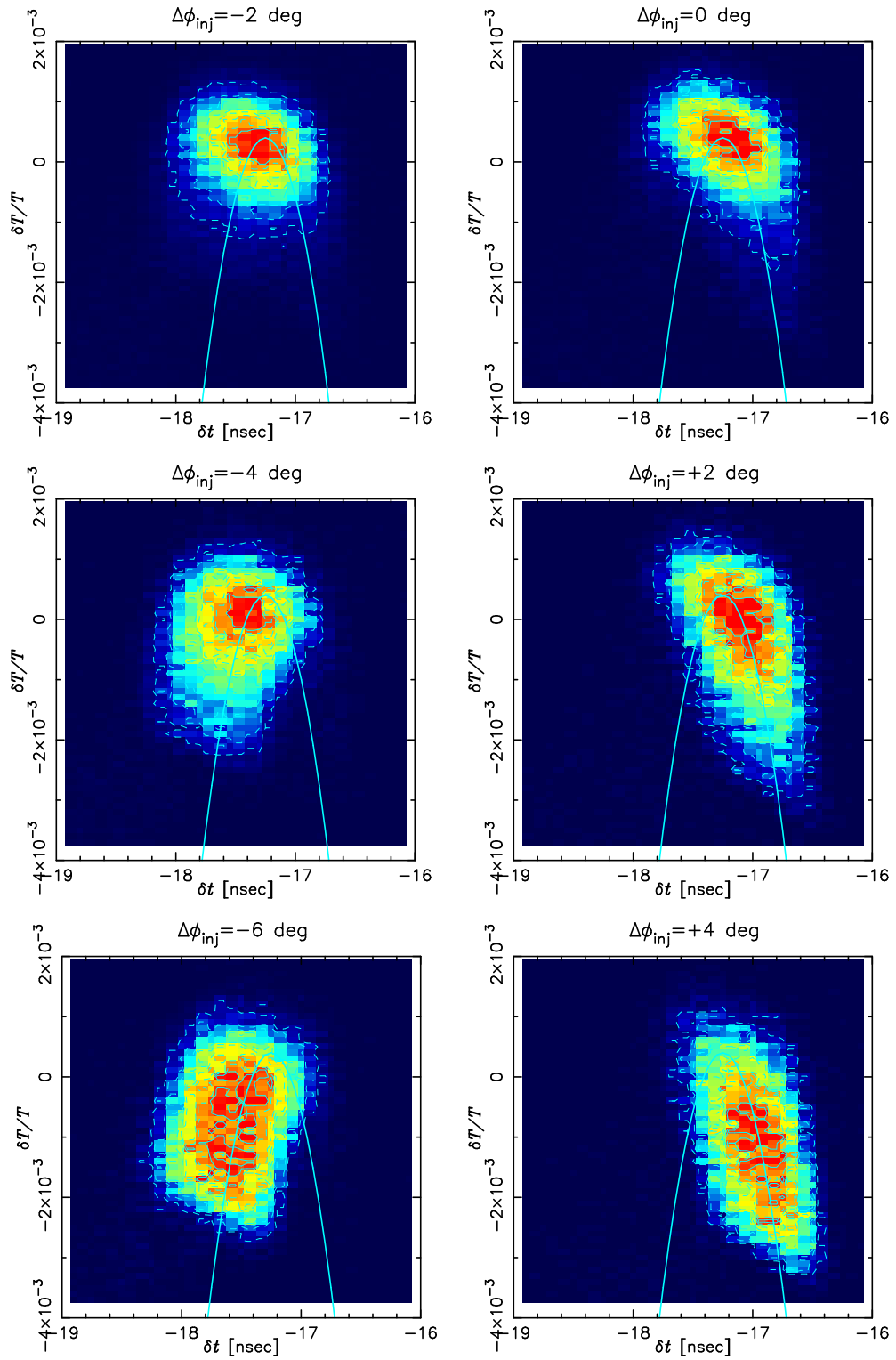


Figure 4.2: Longitudinal emittances of 3800-MeV  $^{40}\text{Ar}$ . The injection phase  $\Delta\phi_{\text{inj}}$  is displaced relative to the RF of the RRC in step of  $2^\circ$ .

compression discussed in Sec. 1.2.6 (upper panel in Fig. 4.3). The effect is directly seen by taking the extraction time relative to the injection (middle panel in Fig. 4.3). The projected spectra corresponding to the lower panel of Fig. 4.3 are presented in Fig. 4.4. The shifts of spectra are deduced from Gaussian peak-fitting and plotted as a function of  $\Delta\phi_{\text{inj}}$  in Fig. 4.5. According to Eq. (1.13), where  $V_{\text{ext}}/V_{\text{inj}} = 1.6$  for the RRC, they are expected to lie on the solid line in Fig. 4.5. It is approximately the case, but the deviation indicates a higher order effect, the origin of which is a future problem.

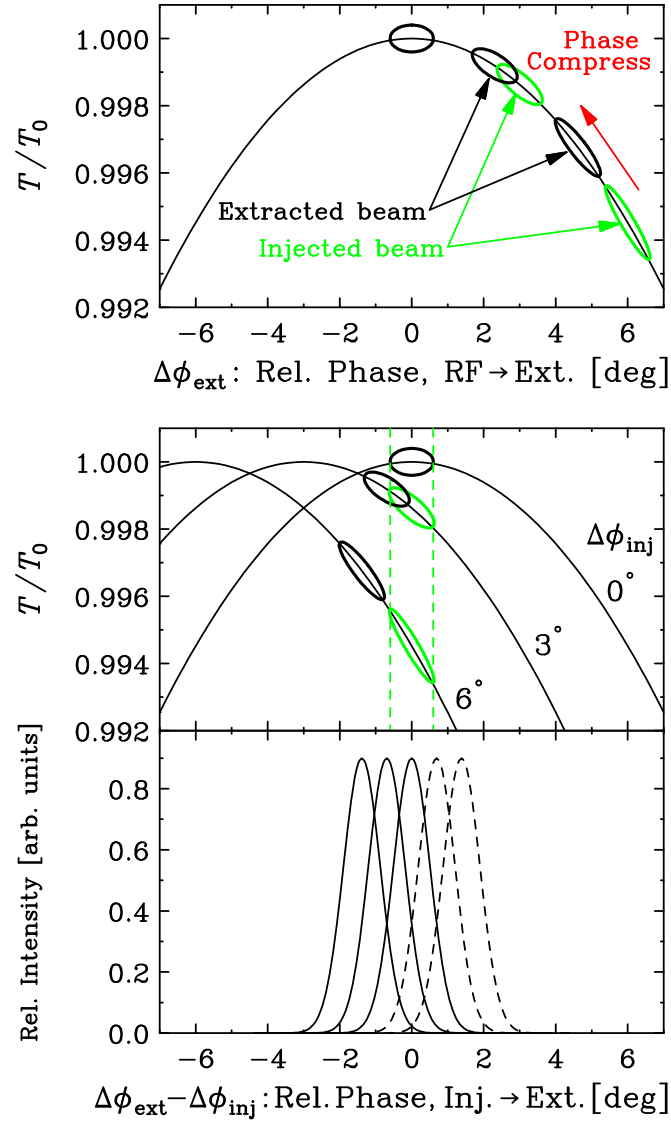


Figure 4.3: Schematic illustration of phase compression effect for the case of narrow-bunched beam. The extraction time is either relative to the RF of the RRC (upper panel) or relative to the injection (lower panel).

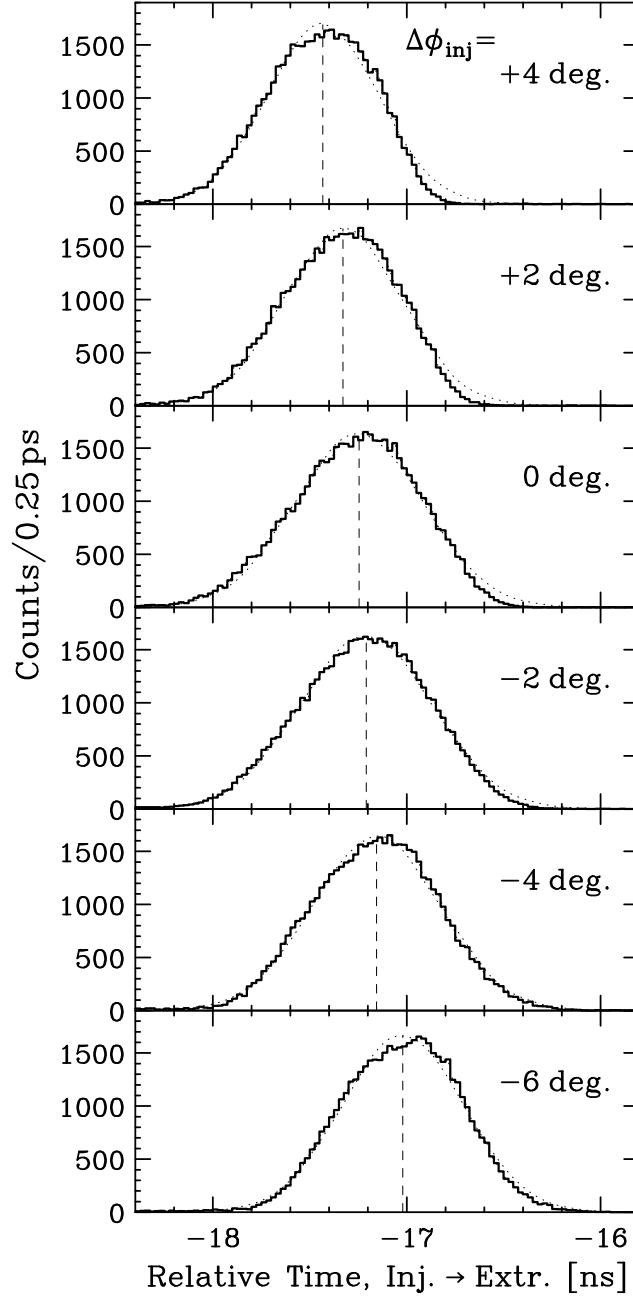


Figure 4.4: Projected spectra of the extraction time relative to the injection. The phase of the RF with respect to the injection,  $\Delta\phi_{\text{inj}}$ , is shifted in step of  $2^\circ$ .

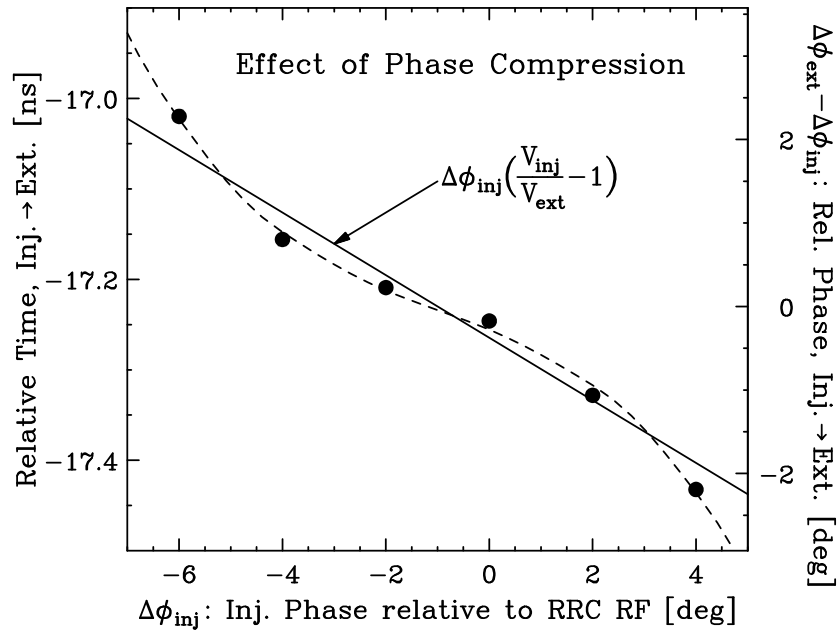


Figure 4.5: Shifts of time spectra deduced from Fig.4.4 plotted as a function of  $\Delta\phi_{inj}$ . The solid line is a prediction from Eq. (1.13). The dashed curve is a third order polynomial for eye-guide.

## 4.3 Longitudinal Emittance of $^{22}\text{Ne}$ Beam

### — case of multi-turn extraction —

The tuning of cyclotrons for the single-turn extraction is not always achieved at RIKEN. In fact, it is sometimes the case that two or three turns are extracted for experiments not requiring a high-quality beam, like ones using a secondary beam. As a case of multi-turn extraction, the longitudinal emittance of 2420-MeV  $^{22}\text{Ne}$  is discussed in this section.

The time structure of the extracted beam relative to the injection time is shown in the upper panel of Fig. 4.6. Two peaks are observed separated by 33.2 ns, one of which would disappear for the case of single-turn extraction. As described in Sec. 2.2, adjacent turns are extracted at different times from the main one by 33.2 ns because  $h_{\text{AVF}}/h_{\text{RRC}} = 2/5$  and  $f_{\text{rf}} = 30.10$  and 15.05 MHz for the RRC and AVF, respectively. Note that the main turn is extracted at an interval of 66.4 ns. The longitudinal emittances for the main and adjacent turns are presented in the middle panel of Fig. 4.6. There are two loci for the adjacent turn, suggesting a mixture of two turns. Together with the main turn, all of the three turns have different  $\delta T$ - $\delta t$  correlations from each other. A possible explanation of this is illustrated in Fig. 4.7. It is assumed that the beam is not injected at the phase of highest voltage and the phase spread is relatively large. A part of the beam distribution is peeled off by the extraction devices at the  $N-1$  turn, the main part at the  $N$  turn and the remaining at the  $N+1$  turn. They are extracted at different phases and accordingly with different  $\delta T$ - $\delta t$  correlations. This idea is supported by the data obtained with the lower Dee voltage by  $2 \times 10^{-3}$  relative to the nominal value. They are shown in the lower panel of Fig. 4.6. Here the beam in the  $N-1$  turn is not extracted and a smaller part of the beam is extracted in the main turn, as expected from the lower panel of Fig. 4.7. This illustration, however, does not explain the data quantitatively and a further study

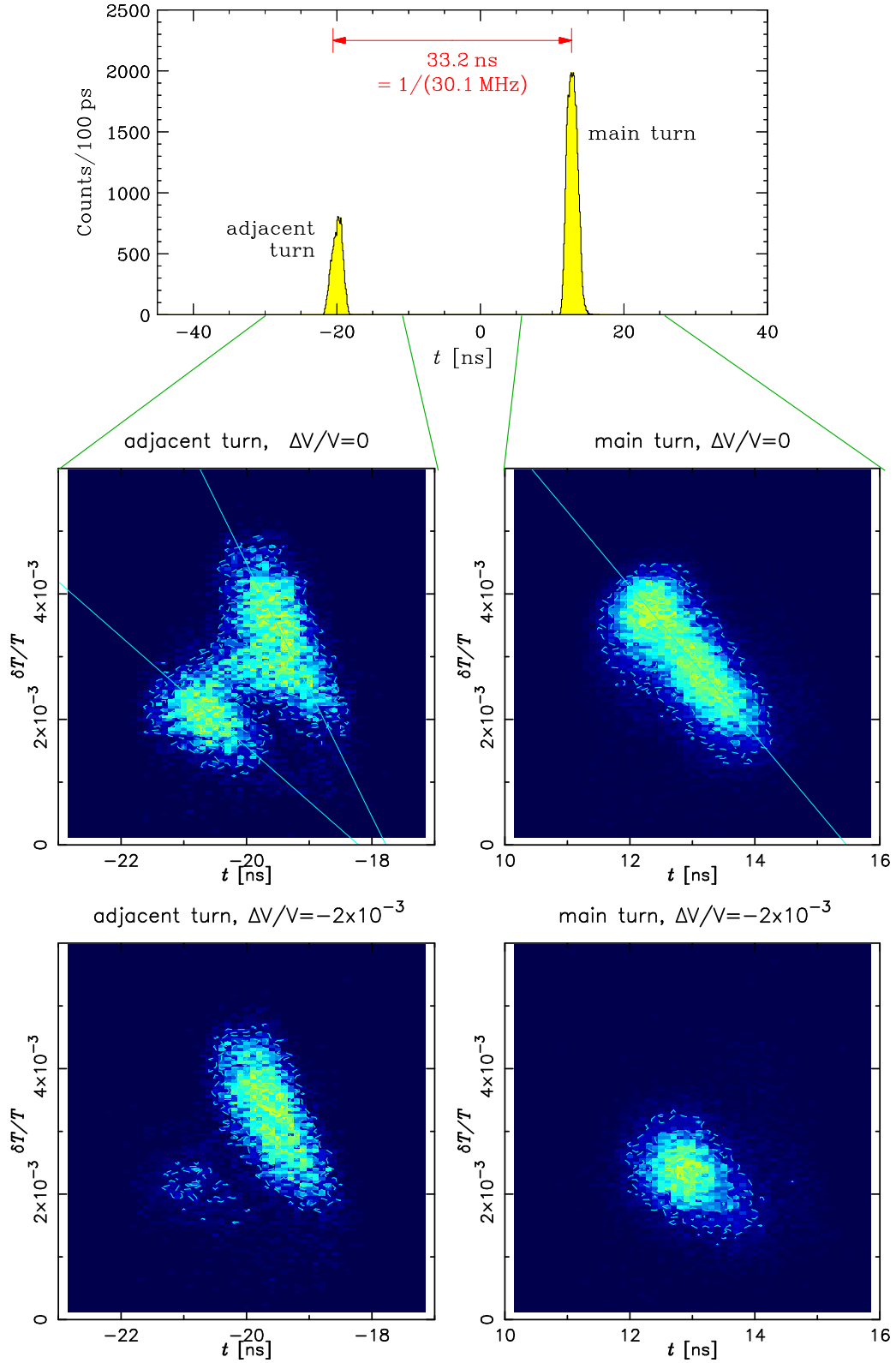


Figure 4.6: Time spectrum (upper panel), the longitudinal emittances for the main and adjacent turns at the nominal Dee voltage (middle panels) and at a slightly lowered Dee voltage (lower panels). Straight lines are for eye-guide.

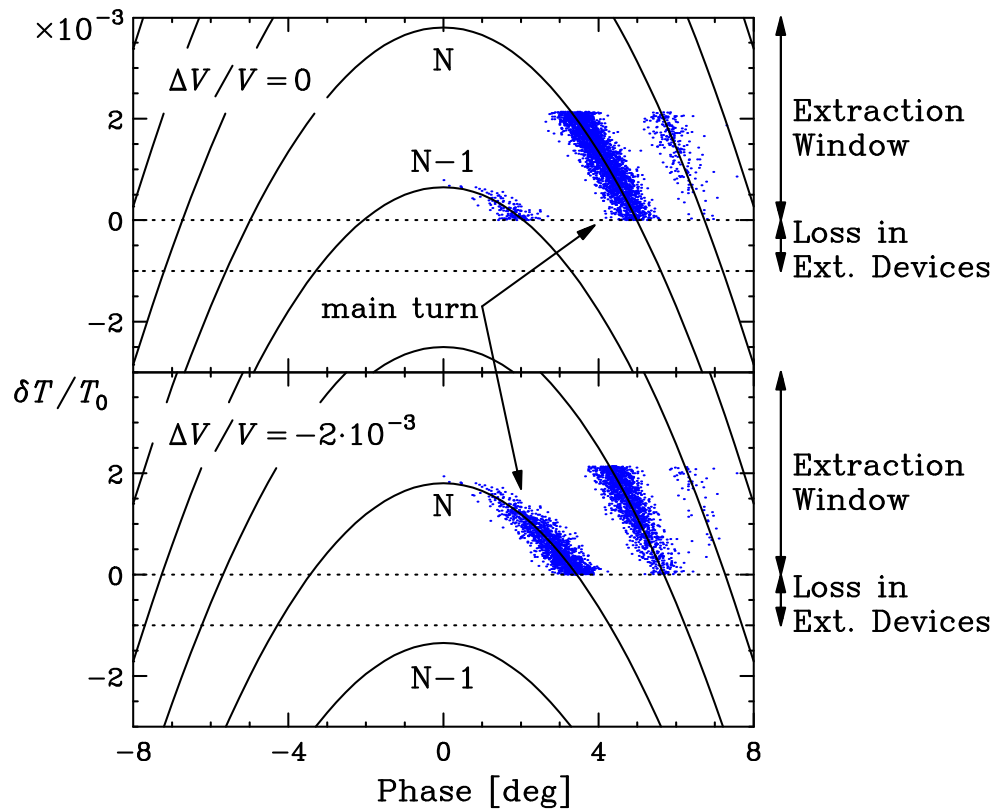


Figure 4.7: Schematic illustration of  $\delta T$ - $\delta t$  correlations for neighboring turns at the nominal Dee voltage (upper panel) and at a slightly lowered Dee voltage (lower panel).

must be made.

# Chapter 5

## Conclusions

It is important to measure the longitudinal emittance of the beam coming from the RRC for successful operations of the new facility, RIBF. A compact and convenient energy detector is desired for routine operations, thus the use of a HPGe detector was proposed and the feasibility of its use with energetic heavy ions was studied. The energy resolution of a HPGe detector for a high-energy heavy ion, 135-MeV/ $A$   $^{14}\text{N}$ , has been measured using a magnetic spectrometer for defining the particle energies. A reasonably good resolution,  $\delta E/E = 6.5 \times 10^{-4}$  (FWHM), has been observed by a HPGe detector with the crystal size as large as  $\phi 70$  mm in diameter and 30 mm in thickness. As a better resolution is expected for smaller crystals, the HPGe is promising as an energy detector for longitudinal emittance measurements.

Using the same magnetic spectrometer, the longitudinal emittances have been measured for the 3800-MeV  $^{40}\text{Ar}$  beam, as a case of the single-turn extraction, and for the 2420-MeV  $^{22}\text{Ne}$  beam, as a case of the multi-turn extraction. For the  $^{40}\text{Ar}$  beam, by displacing the RF phase of the RRC from  $-6^\circ$  to  $+4^\circ$  in step of  $2^\circ$ , a quadratic correlation reflecting the sinusoidal RF voltage as well as the effect of phase compression have been observed. The time spread, however, was larger than expected from the detector resolution and acceleration mechanism. Its origin should

be investigated to observe the correlation more clearly. For the  $^{22}\text{Ne}$  beam, it was found from the time structure of the beam that several turns were extracted. Besides, the longitudinal emittance had a structure suggesting a mixture of different turns. An illustrative explanation has been proposed for identifying each turn. Data with a different Dee voltage are consistent with this idea. However, a further study must be made to obtain a quantitative understanding.

In conclusion, it has been demonstrated that the measurement of longitudinal emittance provides rich information on the acceleration condition and will be very helpful for the beam tuning of the present and new facilities.

# Chapter 6

## Future Prospects

Aiming at a higher energy resolution, a new HPGe detector with a small crystal and a thin Be window had been ordered to Princeton Gammatech, Inc. (Fig. 6.1). The specification is summarized in Table 6.1. The experiment of  $^{22}\text{Ne}$  in October, 2003, was originally proposed to test the resolution of this detector, but, unfortunately, the product was not delivered in time for the experiment. This is going to be performed in this December.

Another test experiment for longitudinal emittance measurement without using a magnetic spectrometer is planned to be performed in the near future. A large scattering chamber, which allows an elastic measurement at  $\theta = 2^\circ$ , has been designed and is under construction.

Since the energy-loss straggling is not negligible even with the plastic scintillator as thin as  $100\ \mu\text{m}$ , the use of a micro-channel plate (MCP) combined with a thin foil for secondary electron production may be examined. Also the improvement of time resolution is critical to see steep correlations more clearly (Sec. 4.2).

After the completion, the system using these detectors will be installed near the exit of the RRC, where the correction of ToF is not required. It will be used for tuning the beam to the present and new facilities as well as for a further study of the

Table 6.1: Specifications of Ge detector (Princeton Gammatech: IGP1010185 Model).

Crystal Type	Diameter	Thickness	Be Window	End Cap Length
Planar Ge	$\phi 10$ mm	10 mm	50.8 $\mu\text{m}$	200 mm
Preamplifier Type	Gain	Energy Range	Vacuum Flange	Dewar Volume
Resistive Feedback	1/60	$\simeq 2$ GeV	CF $\phi 70$ mm	7.5 $\ell$

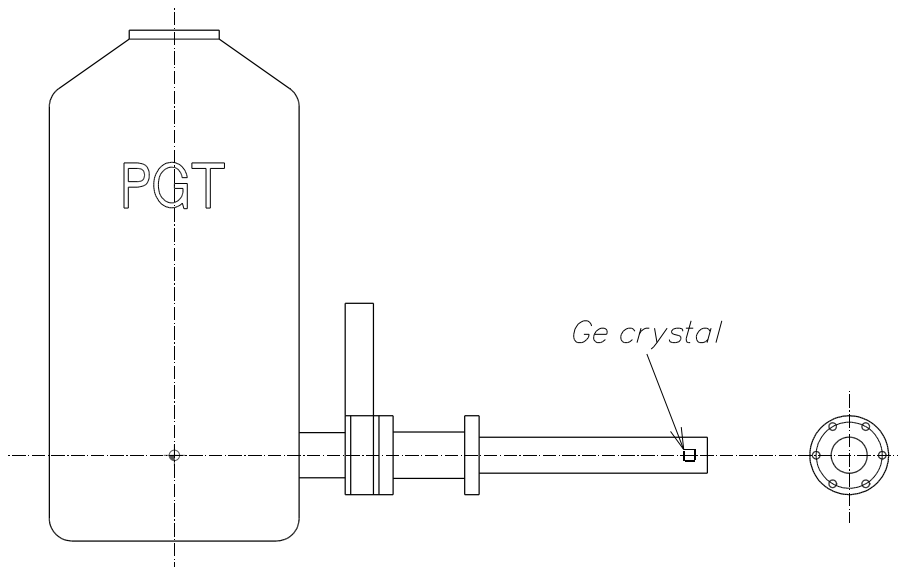


Figure 6.1: Overview of the newly fabricated HPGe detector.

beam from the RRC. Particularly important for the operation of the new facility is a study of 60-MeV/ $A$  beams, which are obtained by using the LINAC as the injector, instead of the AVF cyclotron, but were not available in the present experiments.

# Appendix A

## Angular Distribution of Elastic Scattering

The knowledge on the elastic scattering cross section is important for designing experiments without using a magnetic spectrometer, but data for heavy ions are scarce. The angular distribution of elastic scattering of  $^{14}\text{N}$  on  $^{197}\text{Au}$  target at  $E/A = 135$  MeV/ $A$  has been obtained in the present experiment. The result of the cross section in the laboratory frame is presented in Fig. A.1. It is remarkable that the cross section varies exponentially and the distribution is much steeper than that of the Coulomb scattering from a point charge (Rutherford scattering). Since the cross section becomes very small at backward angles, it will be appropriate to make measurements at  $\theta = 2^\circ\text{--}3^\circ$  in this energy region. The counting rate  $dY/dt$  is related to the cross section  $d\sigma/d\Omega_{\text{lab}}$  by

$$\frac{dY}{dt} = In \frac{d\sigma}{d\Omega_{\text{lab}}} \Delta\Omega_{\text{lab}}, \quad (\text{A.1})$$

where  $I$  denotes the beam intensity,  $n$  the thickness of target and  $\Delta\Omega_{\text{lab}}$  the detector solid angle.

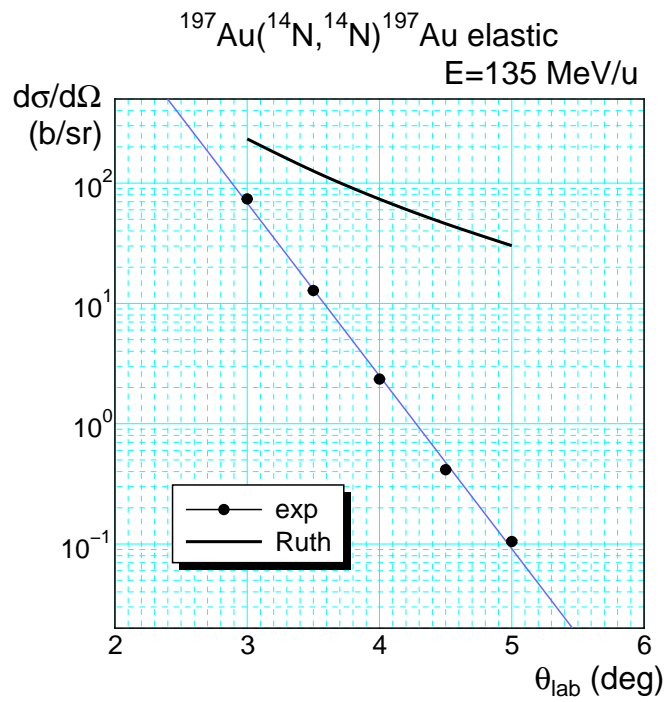


Figure A.1: Angular distribution of  $^{197}\text{Au}(^{14}\text{N}, ^{14}\text{N})^{197}\text{Au}$  elastic scattering at  $E/A = 135$  MeV/ $A$  compared with Rutherford scattering. The exponential line is for eye-guide.

# Acknowledgement

First of all, I would like to express my appreciation to Prof. Martin Berz for preparing the fascinating course of VUBeam and for his continuous support during my study. I am deeply indebted to Dr. Akira Goto, the chief of Beam Dynamics Division at RIKEN Accelerator Research Facility, for providing me an opportunity to make this study. I am grateful to Prof. Toshio Kobayashi at Tohoku University who kindly loaned us the HPGe detector, allowed us to modify the preamplifier and participated in the experiment. Also my thanks go to Prof. Hiroyuki Okamura at Saitama University (presently at Tohoku University) who has been sincerely concerned about me and gave me countless pieces of advice and comment in the course of the experiment, data analysis and writing of this thesis. Theoretical discussions on the experimental results with Dr. Nobuhisa Fukunishi are gratefully acknowledged. I sincerely appreciate the help from Dr. Naruhiko Sakamoto, who provided me a supportive environment for learning about accelerator concepts and made my life at RIKEN delightful. I would like to thank Dr. Hiromichi Ryuto for his support in the experiments and for his careful reading of my thesis. I am thankful to Dr. Kimiko Sekiguchi-Sakaguchi who participated in the experiments and always cheered me heartily. I wish to express my gratitude to all the staff members of the RIKEN Accelerator Research Facility, particularly to the RIKEN cyclotron crew for their excellent machine operation, to Dr. Yasushige Yano, the director of the RIKEN Accelerator Research Facility, who generously accepted me for making a study at RIKEN, and to Dr. Masayuki Kase

for his arrangement of the experiments. I am grateful to Prof. Harry Weerts for his serving my defense committee and for his perceptive comments on my thesis. I am much obliged to Prof. Kyoko Makino for her cordial advice through the course of the study and for her serving my defense committee. Last but not least, I would like to thank my family with my whole heart for their encouragement.

# BIBLIOGRAPHY

- [1] H. Wiedemann, *Particle Accelerator Physics I & II*, second edition, Springer-Verlag, 1998.
- [2] Mario Conte and William W MacKay, *AN INTRODUCTION TO THE PHYSICS OF PARTICLE ACCELERATORS*, first edition, World Scientific Publishing Co. Pte. Ltd, 1991.
- [3] J. I. M. Botman and H. L. Hadedoorn, *EXTRACTION FROM CYCLOTRONS*, report CERN 96-02 article/p169
- [4] B. Martin, R. C. Sethi and K. Ziegler, *Measurements and Studies of the Longitudinal Phase Space at VICKSI*, unpublished.
- [5] V. S. Pandit, *Characteristics of the cyclotron beam in the longitudinal phase space*, Nucl. Instr. and Meth. A **414** (1998) 127.
- [6] R. W. Müller and R. W. Mahrt, *Phase compression and phase dilatation in the isochronous cyclotron*, Nucl. Instr. and Meth. **86** (1970) 241.
- [7] W. Joho, *Application of the phase compression-phase expansion effect for isochronous storage rings*, Particle Accelerators, **6** (1974) 41.
- [8] W. R. Leo, *Techniques for Nuclear and Particle Physics Experiments*, second edition, Springer-Verlag, 1994.
- [9] G. F. Knoll, *Radiation Detection and Measurement*, third edition, John Willy & Sons, 2000.
- [10] D. L. Friesel, B. S. Flanders and R. H. Pehl, *A variable geometry high-purity germanium detector telescope system for use with intermediate energy charged particles*, Nucl. Instr. and Meth., **207** (1983) 403.
- [11] M. Kurokawa *et al.*, *Radiation Damage Factor for Ion-Implanted Silicon Detectors Irradiated with Heavy Ions*, IEEE Trans. Nucl. Sci., **42** (1995) 163.
- [12] T. Ichihara *et al.*, *Spin-Isospin Resonances Observed in the ( $d, {}^2\text{He}$ ) and ( ${}^{12}\text{C}, {}^{12}\text{N}$ ) Reactions at  $E/A = 135 \text{ MeV}$* , Nucl. Phys. **A569** (1994) 287c.

- [13] A. Goto *et al.*, *Beam test and operation of the flattop acceleration system in the RIKEN AVF cyclotron*, RIKEN Accel. Prog. Rep. **36** (2003) 287.
- [14] D. C. Carey, K. L. Brown and F. Rothacker, *Third-Order TRANSPORT with MAD Input, A Computer Program for Designing Charged Particle Beam Transport Systems*, FERMILAB-Pub-98/310, SLAC-R-530 and UC-414.
- [15] H. Okamura, *Fast data acquisition system for the spectrometer SMART at RIKEN*, Nucl. Instr. and Meth., A **443** (2000) 194.
- [16] M. Berz and J. Hoefkens, *COSY INFINITY Version 8.1 Programming Manual*, Technical Report MSUCL-1196 (2001), National Superconducting Cyclotron Laboratory, Michigan State University; K. Makino and M. Berz, *COSY INFINITY version 8*, Nucl. Instr. and Meth. A **427** (1999) 338.